

# Three-generation study of neutrino spin-flavor conversion in supernova and implication for neutrino magnetic moment

Shin'ichiro Ando<sup>1,\*</sup> and Katsuhiko Sato<sup>1,2</sup>

<sup>1</sup>*Department of Physics, School of Science,  
the University of Tokyo, 7-3-1 Hongo,*

*Bunkyo-ku, Tokyo 113-0033, Japan*

<sup>2</sup>*Research Center for the Early Universe,*

*School of Science, the University of Tokyo,*

*7-3-1 Hongo, Bunkyo-ku, Tokyo 113-0033, Japan*

(Dated: July 23, 2002; January 22, 2003, revised)

## Abstract

We investigate resonant spin-flavor (RSF) conversions of supernova neutrinos which are induced by the interaction of neutrino magnetic moment and supernova magnetic fields. From the formulation which includes all three-flavor neutrinos and anti-neutrinos, we give a new crossing diagram that includes not only ordinary MSW resonance but also magnetically-induced RSF effect. With the diagram, it is found that four conversions occur in supernova, two are induced by the RSF effect and two by the pure MSW. We also numerically calculate neutrino conversions in supernova matter, using neutrino mixing parameters inferred from recent experimental results and a realistic supernova progenitor model. The results indicate that until 0.5 seconds after core bounce, the RSF-induced  $\bar{\nu}_e \leftrightarrow \nu_\tau$  transition occurs efficiently (adiabatic resonance), when  $\mu_\nu \gtrsim 10^{-12} \mu_B (B_0/5 \times 10^9 \text{G})^{-1}$ , where  $B_0$  is the strength of the magnetic field at the surface of iron core. We also evaluate the energy spectrum as a function of  $\mu_\nu B_0$  at the SuperKamiokande detector and the Sudbury Neutrino Observatory using the calculated conversion probabilities, and find that the spectral deformation might have possibility to provide useful information on neutrino magnetic moment as well as magnetic field strength in supernovae.

PACS numbers: 95.85.Ry, 14.60.Pq, 13.40.Er, 97.10.Cv, 97.60.Bw

---

\*E-mail: ando@utap.phys.s.u-tokyo.ac.jp

## I. INTRODUCTION

The properties of neutrinos attract a strong attention since neutrinos alone are the elementary particles showing the evidence of new physics beyond the standard model. In particular, recent experiments of the SuperKamiokande (SK) detector [1] and the Sudbury Neutrino Observatory (SNO) [2] have shown that neutrino have non-zero mass and mixing angles by solar [3, 4, 5, 6] and atmospheric [7, 8] neutrino data. These neutrino oscillation experiments enable us to constrain the squared mass difference between mass eigenstates and mixing angles. The solar neutrino experiments strongly support the matter-induced large mixing angle (LMA) solution ( $\Delta m_{12}^2 = 2 - 10 \times 10^{-5} \text{ eV}^2$ ,  $\tan^2 \theta_{12} = 0.25 - 0.5$  [6]) and the atmospheric neutrino experiments have proved that  $\nu_\mu$  and  $\nu_\tau$  are maximally mixing ( $\Delta m_{23}^2 = 2 - 5 \times 10^{-3} \text{ eV}^2$ ,  $\sin^2 2\theta_{23} > 0.88$  [8]). However, there are several parameters which are not sufficiently constrained. One such parameter is  $\theta_{13}$ , for which only upper bound is known from reactor experiment [9] ( $\sin^2 \theta_{13} \lesssim 0.1$ ). In addition, the nature of neutrino mass hierarchy (normal or inverted) is also matter of controversy.

There is another astrophysical source of neutrinos, or supernova. Neutrino burst from the next Galactic core-collapse supernova will be captured by the present underground detectors, such as SK and SNO. It is widely believed that the detected events will provide rich information not only on the mechanism of supernovae but also on the physical properties of neutrinos themselves. In fact, neutrino signals from SN1987A which were detected by the Kamiokande [10] and IMB [11] detectors permitted many discussions about the fundamental properties of neutrinos [12, 13, 14], although the detected event numbers were quite small (11 for Kamiokande, 8 for IMB). What we can learn from the next Galactic supernova is considered in many articles (for a review, see Ref. [15]). For example, we can constrain the properties of neutrino oscillation such as  $\theta_{13}$  and the mass hierarchy [16, 17].

In addition to neutrino mass, non-zero magnetic moment is another nature of neutrinos beyond the standard model. The most stringent upper bound of the neutrino magnetic moment is obtained from cooling argument: any new physics that would enhance the neutrino diffusion, such that the cooling time drops below the observed duration, must be excluded. The recently revised upper bound is  $\mu_\nu \lesssim 1 - 4 \times 10^{-12} \mu_B$  [18], where  $\mu_B$  is the Bohr magneton. The above value is several orders of magnitude more stringent than the existing limit from reactor [19] and solar neutrino experiments [20, 21, 22], and comparable to the

bound from globular cluster red giant cooling arguments [23], which give  $\mu_\nu \lesssim 3 \times 10^{-12} \mu_B$ . On the other hand, from the minimally-extended standard model calculation, we obtain  $\mu_\nu \simeq 3 \times 10^{-19} \mu_B (m_\nu / 1 \text{ eV})$ , which is many orders of magnitude smaller than the current experimental upper bounds. However, some particle physics models have been proposed to induce a larger magnetic moment of order  $\sim 10^{-11} \mu_B$  [24], which is comparable to the current upper bounds.

If neutrinos have the non-zero magnetic moment, it leads to precession between left- and right-handed neutrinos in sufficiently strong magnetic fields expected in the inner region of the core-collapse supernova [25, 26]. In general, non-diagonal elements of the magnetic moment matrix are possible and neutrinos can be changed into different flavors and chiralities [27]. Furthermore, with the additional effect of the coherent forward scattering by matter, neutrinos can be resonantly converted into those with different chiralities [28] by a mechanism similar to the well known Mikheyev-Smirnov-Wolfenstein (MSW) effect [29, 30]. This resonant spin-flavor (RSF) conversion induced by the neutrino magnetic moment in the supernova has been studied by many authors [28, 31, 32, 33, 34, 35, 36, 37, 38]. Almost all these earlier publications considered the RSF conversions between two-flavor neutrinos ( $\bar{\nu}_e \leftrightarrow \nu_\mu$ ). However, since all three-flavor neutrinos and anti-neutrinos are emitted from the supernova core, we should calculate conversion probabilities using three-flavor formulation to obtain the spectrum of the neutrinos in the detectors. Fortunately, our knowledge of the neutrino mixing parameters permits the three-flavor analyses, which have not been considered because of many unknown parameters in those days.

In this paper, we study the RSF effect in detail, including three flavor neutrinos and anti-neutrinos. Particularly, a new crossing diagram, which deals with both MSW and RSF effects, is given. From the diagram, we find that the combination of the MSW and the RSF effects makes crossing schemes very interesting to investigate, and the expected flux would be different from that obtained in the case of pure MSW or pure RSF effect. In addition, we calculate numerically the conversion probabilities of neutrinos and anti-neutrinos in the supernova using three-flavor formulation. In the calculations, we adopt the latest neutrino mixing parameters, which are constrained by the solar and the atmospheric neutrino experiments, and assume the normal mass hierarchy. However, there are two

unknown parameters of neutrinos,  $\mu_\nu$  and  $\theta_{13}$ <sup>1</sup>. For  $\mu_\nu$ , we assume the value  $10^{-12}\mu_B$ <sup>2</sup>, and for  $\theta_{13}$ , two large and small values ( $\sin^2 2\theta_{13} = 0.04, 10^{-6}$ ). Using the calculated conversion probabilities, we give the expected energy spectra at SK and SNO detectors, which show various behaviors as we change the value of  $\mu_\nu B$ . Finally, we discuss the model uncertainties and how to obtain the implication for the value of neutrino magnetic moment from the obtained energy spectra.

This paper is organized as follows. In Section II, we give the formulation used in our calculation, which includes all three flavor neutrinos and anti-neutrinos. In Section III, the neutrino oscillation models and supernova models (original neutrino spectrum, density,  $Y_e$ , and magnetic field profiles) considered in this paper are illustrated and their validity is also discussed. In Section IV, we give a new crossing diagram, with which qualitative discussions concerning neutrino conversions in supernova matter become possible. The numerically calculated conversion probabilities and energy spectra at SK and SNO are shown in Section V. Finally, detailed discussions on model uncertainties and how to obtain the implication for neutrino magnetic moment are presented in Section VI.

## II. FORMULATION

The interaction of the magnetic moment of neutrinos and magnetic fields is described by

$$\langle (\nu_i)_R | H_{\text{int}} | (\nu_j)_L \rangle = \mu_{ij} B_\perp, \quad (1)$$

where  $\mu_{ij}$  is the component of the neutrino magnetic moment matrix,  $B_\perp$  the magnetic field transverse to the direction of propagation,  $(\nu)_R$  and  $(\nu)_L$  the right- and left-handed neutrinos, respectively, and  $i$  and  $j$  denote the flavor eigenstate of neutrinos, i.e.,  $e$ ,  $\mu$ , and  $\tau$ . If neutrinos are the Dirac particles, right-handed neutrinos and left-handed anti-neutrinos are undetectable (sterile neutrinos), since they do not interact with matter. The spin-flavor conversion into these sterile neutrinos suffers strong constraints from observation of neutrinos from SN1987A [32, 34, 39]. On the other hand, if neutrinos are the Majorana particles,

---

<sup>1</sup> There are many unknown properties in supernova physics, such as density profile,  $Y_e$ , and magnetic field. We give in Section III the adopted properties in our calculation.

<sup>2</sup> Since the neutrino magnetic moment enters into the evolution equation only in the combination  $\mu_\nu B$  (see Section II), the results would also apply to any other value of  $\mu_\nu$  provided that the supernova magnetic field strength is rescaled accordingly.

$\nu_R$ 's are identical to anti-particles of  $\nu_L$ 's and interact with matter, and the constraint above becomes considerably weak. In this paper, we assume that neutrinos are Majorana particles. The diagonal magnetic moments is forbidden for the Majorana neutrinos, and therefore, only the conversion between different flavors is possible, e.g.,  $(\bar{\nu}_e)_R \leftrightarrow (\nu_{\mu,\tau})_L$ .

The coherent forward scattering with matter induces the effective potential for neutrinos, which is calculated using weak interaction theory. The effective potential due to scattering with electrons is given as

$$V_{\pm\pm} = \pm\sqrt{2}G_F \left( \pm\frac{1}{2} + 2\sin^2\theta_W \right) n_e, \quad (2)$$

where  $n_e$  is electron number density,  $G_F$  the Fermi coupling constant, and  $\theta_W$  the Weinberg angle. The  $\pm$  sign in front refers to  $\nu$  (+) and  $\bar{\nu}$  (−) and that in the parentheses to  $\nu_e$  (+) and  $\nu_{\mu,\tau}$  (−). The difference between  $e$  and  $\mu, \tau$  neutrinos comes from the existence of charged-current interaction. The subscript  $\pm\pm$  of  $V$  refers to the first and the second  $\pm$  sign. The ordinary MSW effect between  $\nu_e$  and  $\nu_{\mu,\tau}$  is caused by the potential difference,  $V_e - V_{\mu,\tau} = V_{++} - V_{+-} = \sqrt{2}G_F n_e$ . To include the RSF effect, which causes the conversion between neutrinos and anti-neutrinos, we should take into account the neutral-current scattering by nucleons:

$$V = \sqrt{2}G_F \left( \frac{1}{2} - 2\sin^2\theta_W \right) n_p - \sqrt{2}G_F \frac{1}{2} n_n, \quad (3)$$

where  $n_p$ ,  $n_n$  are proton and neutron number density, respectively. For neutrinos we add  $+V$  to the potential and for anti-neutrinos  $-V$ . Therefore, the RSF conversion between  $\bar{\nu}_e$  and  $\nu_{\mu,\tau}$  obeys the potential difference

$$\begin{aligned} \Delta V &\equiv V_{\bar{e}} - V_{\mu,\tau} \\ &= (V_{-+} - V) - (V_{+-} + V) \\ &= \sqrt{2}G_F \frac{\rho}{m_N} (1 - 2Y_e), \end{aligned} \quad (4)$$

where  $\rho$  is the density,  $m_N$  the nucleon mass, and  $Y_e = n_e/(n_e + n_n)$  is the number of electrons per baryon. (When we obtain Eq. (4), we assumed charge neutrality  $n_e = n_p$ .)

#### A. The simplest case: $\bar{\nu}_e \leftrightarrow \nu_\mu$ conversion

In this subsection, we give the simplest formulation between  $\bar{\nu}_e$  and  $\nu_\mu$ , and consider the properties of the RSF conversion. The time evolution of the mixed state of  $\bar{\nu}_e$  and  $\nu_\mu$  is

described by the Schrödinger equation

$$i \frac{d}{dr} \begin{pmatrix} \bar{\nu}_e \\ \nu_\mu \end{pmatrix} = \begin{pmatrix} 0 & \mu_{e\mu} B_\perp \\ \mu_{e\mu} B_\perp & \Delta H \end{pmatrix} \begin{pmatrix} \bar{\nu}_e \\ \nu_\mu \end{pmatrix}, \quad (5)$$

where  $r$  is the radius from the center of the star,  $\mu_{e\mu}$  the transition magnetic moment, and  $\Delta H$  is defined by

$$\Delta H \equiv \frac{\Delta m_{12}^2}{2E_\nu} \cos 2\theta_{12} - \Delta V. \quad (6)$$

The resonance occurs when  $\Delta H = 0$ , thus, the necessary condition is  $Y_e < 0.5$ . (If  $Y_e > 0.5$ , the  $\nu_e \leftrightarrow \bar{\nu}_\mu$  conversion occurs conversely, at almost the same place.) Several earlier authors [35, 36] pointed out that the RSF conversion occurs quite efficiently in the region above the iron core and below the hydrogen envelope of collapsing stars, namely, in the “isotopically neutral region” (O+Si, O+Ne+Mg, O+C, and He layers), in which the value of  $Y_e$  is slightly less than 0.5 [typically,  $(1 - 2Y_e) \sim 10^{-4} - 10^{-3}$ ]. Actually, the pre-supernova model used in our calculation have the similar profile, as is shown in Section III C.

When the resonance is adiabatic (or when the density is slowly changing at that point and the magnetic field is strong enough), the significant conversion occurs. The adiabaticity of the RSF conversion can be derived by the same argument used in the case of the MSW conversion [30, 35]. It is given by

$$\gamma_{\bar{e}\mu}^{\text{RSF}} = \frac{(2\mu_{e\mu} B_\perp)^2}{|d\Delta V/dr|} \Big|_{\text{res}}, \quad (7)$$

where the subscript “res” means that the value is evaluated at the resonance point. Therefore, if the magnetic field is sufficiently strong at the resonance point, the  $\bar{\nu}_e \leftrightarrow \nu_\mu$  conversion occurs completely.

At the end of this subsection, we discuss the possibility that  $\nu_e \leftrightarrow \bar{\nu}_\mu$  conversion occurs in solar magnetic field. There are several works examining the RSF conversion as a solution to the solar neutrino problem [40]. In this paper, however, we postulate that the solution to the solar neutrino problem is given by the ordinary MSW effect (LMA solution). In fact, if we take the mixing parameters of LMA ( $\Delta m_{12}^2 = 2 - 10 \times 10^{-5} \text{ eV}^2$ ,  $\tan^2 \theta_{12} = 0.25 - 0.5$ ) in calculating the RSF resonance condition  $\Delta H = 0$ , the required density is found to be larger than the central density of the Sun. (In this calculation, the sign of  $\Delta V$  is changed in Eq. (6), since  $Y_e > 0.5$  in the Sun. This corresponds to  $\nu_e \leftrightarrow \bar{\nu}_\mu$  conversion.)

## B. Three-flavor formulation

Here, we present the three-flavor (six-component) formulation of neutrino mixing by

$$i \frac{d}{dr} \begin{pmatrix} \nu \\ \bar{\nu} \end{pmatrix} = \begin{pmatrix} H_0 & B_\perp M \\ -B_\perp M & \bar{H}_0 \end{pmatrix} \begin{pmatrix} \nu \\ \bar{\nu} \end{pmatrix}, \quad (8)$$

where

$$\nu = \begin{pmatrix} \nu_e \\ \nu_\mu \\ \nu_\tau \end{pmatrix}, \quad \bar{\nu} = \begin{pmatrix} \bar{\nu}_e \\ \bar{\nu}_\mu \\ \bar{\nu}_\tau \end{pmatrix}, \quad (9)$$

$$H_0 = \frac{1}{2E_\nu} U \begin{pmatrix} 0 & 0 & 0 \\ 0 & \Delta m_{12}^2 & 0 \\ 0 & 0 & \Delta m_{13}^2 \end{pmatrix} U^\dagger + \begin{pmatrix} V_{++} + V & 0 & 0 \\ 0 & V_{+-} + V & 0 \\ 0 & 0 & V_{+-} + V \end{pmatrix}, \quad (10)$$

$$\bar{H}_0 = \frac{1}{2E_\nu} U \begin{pmatrix} 0 & 0 & 0 \\ 0 & \Delta m_{12}^2 & 0 \\ 0 & 0 & \Delta m_{13}^2 \end{pmatrix} U^\dagger + \begin{pmatrix} V_{-+} - V & 0 & 0 \\ 0 & V_{--} - V & 0 \\ 0 & 0 & V_{--} - V \end{pmatrix}, \quad (11)$$

$$U = \begin{pmatrix} U_{e1} & U_{e2} & U_{e3} \\ U_{\mu1} & U_{\mu2} & U_{\mu3} \\ U_{\tau1} & U_{\tau2} & U_{\tau3} \end{pmatrix} = \begin{pmatrix} c_{12}c_{13} & s_{12}c_{13} & s_{13} \\ -s_{12}c_{23} - c_{12}s_{23}s_{13} & c_{12}c_{23} - s_{12}s_{23}s_{13} & s_{23}c_{13} \\ s_{12}s_{23} - c_{12}c_{23}s_{13} & -c_{12}s_{23} - s_{12}c_{23}s_{13} & c_{23}c_{13} \end{pmatrix}, \quad (12)$$

$$M = \begin{pmatrix} 0 & \mu_{e\mu} & \mu_{e\tau} \\ -\mu_{e\mu} & 0 & \mu_{\mu\tau} \\ -\mu_{e\tau} & -\mu_{\mu\tau} & 0 \end{pmatrix}, \quad (13)$$

and  $c_{ij} = \cos \theta_{ij}$ ,  $s_{ij} = \sin \theta_{ij}$ . (We assume CP phase  $\delta = 0$  in Eq. (12) for simplicity.)

The resonant flavor conversion occurs when the two diagonal elements in matrix in Eq. (8) have the same value. There are five such resonance points, which are for  $\nu_e \leftrightarrow \nu_\mu$  (MSW-L),  $\nu_e \leftrightarrow \nu_\tau$  (MSW-H),  $\bar{\nu}_e \leftrightarrow \nu_\mu$  (RSF-L),  $\bar{\nu}_e \leftrightarrow \nu_\tau$  (RSF-H), and  $\bar{\nu}_\mu \leftrightarrow \nu_\tau$  conversions. Suffixes “-L” and “-H” attached to “MSW” and “RSF” indicate whether the density at the resonance points are lower or higher. Hereafter, we neglect  $\bar{\nu}_\mu \leftrightarrow \nu_\tau$  conversion, since it is always nonadiabatic as well as including this makes discussion further complicated.

### III. MODELS

#### A. Neutrino parameters

We adopt the neutrino mixing parameters introduced to explain the observations of the solar and the atmospheric neutrino experiments [3, 4, 5, 6, 7, 8], and assume the normal mass hierarchy. From the atmospheric neutrino experiments, we use the values [8]

$$\Delta m_{13}^2 = 2.8 \times 10^{-3} \text{ eV}^2, \quad \sin^2 2\theta_{23} = 1.0, \quad (14)$$

and from the solar neutrino experiments [6],

$$\Delta m_{12}^2 = 5.0 \times 10^{-5} \text{ eV}^2, \quad \tan^2 \theta_{12} = 0.34, \quad (15)$$

in our calculations. For  $\theta_{13}$ , which is not sufficiently constrained, we adopt two large and small values,

$$\sin^2 2\theta_{13} = 0.04, \quad 1.0 \times 10^{-6}, \quad (16)$$

where each value causes the adiabatic and nonadiabatic MSW-H conversions, respectively.

As for neutrino magnetic moment, there are three transition moments for Majorana neutrino (Eq. (13)). We assume that all of them are near the present upper bound (i.e.,  $\mu_{ij} = 10^{-12} \mu_B$ ). However, as we will show in Section III D,  $\mu_{e\tau}$  alone governs results.

#### B. Original spectrum of neutrinos

We use a realistic model of a collapse-driven supernova by the Lawrence Livermore group [41] to calculate the neutrino energy spectrum at production. We show in Fig. 1 the time-integrated energy spectra of neutrinos (see Ref. [42] for detail), where the distance to the supernova is set to 10 kpc. (For discussions from here, we adopt this assumption,  $D = 10$  kpc.) Both the flux integrated over entire time during neutrino burst and that integrated until 0.5 seconds after core bounce are shown in the same figure. Although the neutrino burst persists  $\sim 10$  seconds, about half of neutrinos are emitted by 0.5 seconds, according to numerical simulation by Lawrence Livermore group [42]. The reason for using time integrated flux until 0.5 seconds is given in the next subsection.



The mean energies are different between flavors:

$$\langle E_{\nu_e} \rangle \simeq 11 \text{ MeV}, \quad (17)$$

$$\langle E_{\bar{\nu}_e} \rangle \simeq 16 \text{ MeV}, \quad (18)$$

$$\langle E_{\nu_x} \rangle \simeq 22 \text{ MeV}, \quad (19)$$

for fully time-integrated spectrum, while for that integrated until 0.5 seconds,

$$\langle E_{\nu_e} \rangle \simeq 11 \text{ MeV}, \quad (20)$$

$$\langle E_{\bar{\nu}_e} \rangle \simeq 14 \text{ MeV}, \quad (21)$$

$$\langle E_{\nu_x} \rangle \simeq 18 \text{ MeV}. \quad (22)$$

This hierarchy of mean energies is explained as follows. Since  $\nu_x$ 's interact with matter only through the neutral-current reactions in supernova, they are weakly coupled with matter compared to  $\nu_e$ 's and  $\bar{\nu}_e$ 's. Thus the neutrino sphere of  $\nu_x$ 's is deeper in the core than that of  $\nu_e$ 's and  $\bar{\nu}_e$ 's, which leads to higher temperatures for  $\nu_x$ 's. The difference between  $\nu_e$ 's and  $\bar{\nu}_e$ 's comes from that the core is neutron rich and  $\nu_e$ 's couples with matter more strongly, through  $\nu_e n \rightarrow e^- p$  reactions.

### C. Supernova progenitor model

We use the precollapse model of massive stars of Woosley and Weaver [43]. The progenitor mass was set to be  $15M_\odot$ , and the metallicity the same as that of the Sun. The upper panel of Fig. 2 shows  $\rho Y_e$  and  $\rho(1-2Y_e)$  profiles of this progenitor model. In the same figure, we also show  $\Delta_{12} \equiv \Delta m_{12}^2 \cos 2\theta_{12}/2\sqrt{2}G_F E_\nu$  and  $\Delta_{13} \equiv \Delta m_{13}^2 \cos 2\theta_{13}/2\sqrt{2}G_F E_\nu$ . At intersections between  $\Delta_{12}, \Delta_{13}$  and  $\rho(1-2Y_e), \rho Y_e$ , the RSF and MSW conversions occur (see Eq. (6)).

However, in fact, since the density profile changes drastically during neutrino burst ( $\sim 10$  sec) owing to shock propagation, we cannot use the static progenitor model when calculating the conversion probability in supernova [44]. We show in Fig. 3 the *time-dependent*  $\rho(1-2Y_e)$  and  $\rho Y_e$  profile calculated by Lawrence Livermore group [45], compared with the static model adopted in our calculation [43]. From the figure, the shock wave changes the  $\rho(1-2Y_e)$  profile in the resonance region, which is responsible for RSF conversions, at  $> 0.5$  seconds after bounce, while that at  $\lesssim 0.5$  seconds is almost the same as the static progenitor model. Thus, from here, we confine our discussion until 0.5 seconds after core bounce, since in that case,

using the static progenitor model is considered to be a good approximation. Calculating for full time-scale during neutrino burst with the time-dependent density and  $Y_e$  profiles makes discussion very complicated, and it is out of scope of this study, while it will be our future work.

#### D. Supernova magnetic field

We assume that the global structure of the magnetic field is a dipole moment and the field strength is normalized at the surface of the iron core with the value of  $10^8 - 10^{10}$  Gauss. The reason for this normalization is as follows. As pointed out by Totani and Sato [36], the global magnetic field normalized at the surface of the newly born neutron star, such as used in Ref. [35], is not a good assumption. It is because that the magnetic fields of a nascent neutron star are hard to affect the far outer region, such as the isotopically neutral region, within the short time scale of neutrino burst. The magnetic fields, therefore, should be normalized by the fields which are static and existent before the core collapse. In addition, as discussed in the previous subsection, since the shock wave does not affect the resonance region at  $\lesssim 0.5$  seconds after bounce, it is also expected that the magnetic field strength at the resonance points is not seriously changed at that time. The strength of such magnetic fields above the surface of the iron core may be inferred from the observation of the surface of white dwarfs, since both are sustained against the gravitational collapse by the degenerate pressure of electrons. The observations of the magnetic fields in white dwarfs show that the strength spreads in a wide range of  $10^7 - 10^9$  Gauss [46]. Taking account of the possibility of the decay of magnetic fields in white dwarfs, it is not unnatural to consider the magnetic fields up to  $10^{10}$  Gauss at the surface of the iron core. Then, in Eq. (8),  $B_\perp = B_0(r_0/r)^3 \sin \Theta$ , where  $B_0$  is the strength of the magnetic field at the equator on the iron core surface,  $r_0$  the radius of the iron core, and  $\Theta$  the angle between the pole of the magnetic dipole and the direction of neutrino propagation. Hereafter, we assume  $\sin \Theta = 1$ .

From the magnetic field, density, and  $Y_e$  profiles of supernova we can calculate the adiabaticity parameter of each resonance points with Eq. (7). The lower panel of Fig. 2 shows adiabaticity parameters of RSF conversions as a function of radius. Those for both  $B_0 = 10^8$  and  $B_0 = 10^{10}$  Gauss, when  $\mu_\nu = 10^{-12} \mu_B$  is assumed, are shown. From the figure, we see that the RSF-H conversion can be adiabatic when the  $B_0 \sim 10^{10}$  G, while the RSF-L conver-

sion is always nonadiabatic under any conditions considered here. Therefore, the values of transition magnetic moment  $\mu_{e\mu}, \mu_{\mu\tau}$  do not matter, while that of  $\mu_{e\tau}$  alone governs results.

#### IV. LEVEL CROSSING SCHEMES AND QUALITATIVE ILLUSTRATIONS

From the formulation which includes three-flavor neutrinos and anti-neutrinos (Eq. (8)), we give a new level crossing diagram, which is an expanded version of the ordinary diagram including MSW resonance alone (see Fig. 5 in Ref. [16]). We show it in Fig. 4, in which the adiabatic conversion means that the neutrinos trace the solid curve at each resonance point (i.e., the mass eigenstate does not flip), while the nonadiabatic conversion the dotted line. The figure clearly includes not only ordinary MSW resonances but also the RSF effects, and it is expected that the combination effect of MSW and RSF makes this scheme very interesting to investigate. From the earlier publications on the MSW effect, we know that the MSW-L is adiabatic for LMA solution, and MSW-H is adiabatic for large  $\theta_{13}$  and nonadiabatic for small  $\theta_{13}$  [16, 17]. The adiabaticity of the RSF-L and RSF-H depends on the magnetic field strength and the density profile at the resonance point (see Eq. (7)), which are given in Section III and Fig. 2.

Here, we qualitatively consider the flavor transition of neutrinos under some simple conditions. At the supernova core, electron neutrinos and anti-neutrinos are produced as the mass eigenstate in matter, owing to large matter potential. The other flavor ( $\mu, \tau$ ) neutrinos and anti-neutrinos at production are not mass eigenstates, however, we can make them by linear combination of these flavor eigenstates. (These states corresponds to  $\nu'_\mu, \nu'_\tau, \bar{\nu}'_\mu, \bar{\nu}'_\tau$  in Fig. 4.) Then, neutrinos and anti-neutrinos of all flavors propagate in supernova matter along the curves in Fig. 4, being affected by four resonances, and appear from the stellar surface as pure vacuum mass eigenstates or their mixing states.

When both the RSF-L and RSF-H are nonadiabatic, the situation is the same as the pure MSW case, i.e., the conversions occurs as

$$\left. \begin{array}{l} \nu_e \rightarrow \nu_3 \quad \bar{\nu}_e \rightarrow \bar{\nu}_1 \\ \nu'_\mu \rightarrow \nu_1 \quad \bar{\nu}'_\mu \rightarrow \bar{\nu}_2 \\ \nu'_\tau \rightarrow \nu_2 \quad \bar{\nu}'_\tau \rightarrow \bar{\nu}_3 \end{array} \right\} \quad (\text{adiabatic MSW-H}),$$

$$\left. \begin{aligned} \nu_e &\rightarrow \nu_2 & \bar{\nu}_e &\rightarrow \bar{\nu}_1 \\ \nu'_\mu &\rightarrow \nu_1 & \bar{\nu}'_\mu &\rightarrow \bar{\nu}_2 \\ \nu'_\tau &\rightarrow \nu_3 & \bar{\nu}'_\tau &\rightarrow \bar{\nu}_3 \end{aligned} \right\} \quad (\text{nonadiabatic MSW-H}).$$

From these considerations, we can estimate the spectral deformation of  $\nu_e$  and  $\bar{\nu}_e$ , which are the easiest to detect at SK and SNO. When the MSW-H is adiabatic, we obtain

$$\begin{aligned} F_e &= |U_{e1}|^2 F_1 + |U_{e2}|^2 F_2 + |U_{e3}|^2 F_3 \\ &= |U_{e1}|^2 F_x^0 + |U_{e2}|^2 F_x^0 + |U_{e3}|^2 F_e^0 \\ &= (1 - |U_{e3}|^2) F_x^0 + |U_{e3}|^2 F_e^0, \end{aligned} \quad (23)$$

$$F_{\bar{e}} = |U_{e1}|^2 F_{\bar{e}}^0 + (1 - |U_{e1}|^2) F_x^0, \quad (24)$$

where  $F_i$  is the flux of the  $i$ -type neutrinos at detection,  $F_i^0$  the flux at production which is shown in Fig. 1, and subscript  $x = \mu, \tau, \bar{\mu}, \bar{\tau}$ , since the flux of these flavors are considered to be the same. With the same manner, for nonadiabatic MSW-H, we obtain

$$F_e = (1 - |U_{e2}|^2) F_x^0 + |U_{e2}|^2 F_e^0, \quad (25)$$

$$F_{\bar{e}} = |U_{e1}|^2 F_{\bar{e}}^0 + (1 - |U_{e1}|^2) F_x^0. \quad (26)$$

When the RSF-H is adiabatic and RSF-L nonadiabatic, which is actually the case for strong magnetic field (see Fig. 2), the same arguments lead to for adiabatic MSW-H:

$$\left\{ \begin{aligned} \nu_e &\rightarrow \nu_3 & \bar{\nu}_e &\rightarrow \nu_2 \\ \nu'_\mu &\rightarrow \nu_1 & \bar{\nu}'_\mu &\rightarrow \bar{\nu}_2 \\ \nu'_\tau &\rightarrow \bar{\nu}_1 & \bar{\nu}'_\tau &\rightarrow \bar{\nu}_3 \end{aligned} \right. ,$$

$$F_e = |U_{e1}|^2 F_x^0 + |U_{e2}|^2 F_{\bar{e}}^0 + |U_{e3}|^2 F_e^0, \quad (27)$$

$$F_{\bar{e}} = F_x^0, \quad (28)$$

and for nonadiabatic MSW-H:

$$\left\{ \begin{aligned} \nu_e &\rightarrow \nu_2 & \bar{\nu}_e &\rightarrow \nu_3 \\ \nu'_\mu &\rightarrow \nu_1 & \bar{\nu}'_\mu &\rightarrow \bar{\nu}_2 \\ \nu'_\tau &\rightarrow \bar{\nu}_1 & \bar{\nu}'_\tau &\rightarrow \bar{\nu}_3 \end{aligned} \right. ,$$

$$F_e = |U_{e1}|^2 F_x^0 + |U_{e2}|^2 F_e^0 + |U_{e3}|^2 F_{\bar{e}}^0, \quad (29)$$

$$F_{\bar{e}} = F_x^0. \quad (30)$$

The adiabatic RSF-H conversion, thus, deforms the energy spectra, and the difference from the case of the pure MSW effect is clear.

## V. RESULTS OF NUMERICAL CALCULATIONS

### A. Conversion probability

We calculated Eq. (8) numerically with adopted models given in Section III, and obtained the conversion probabilities for each flavor. Figure 5 shows those for  $\bar{\nu}_e$  (upper panel (a)) and  $\nu_\mu$  (lower panel (b)), under the condition that  $B_0 = 4 \times 10^9$  G,  $E_\nu = 20$  MeV, and  $\sin^2 2\theta_{13} = 0.04$ . Since  $\nu_\tau$ 's ( $\bar{\nu}_\tau$ 's) are maximally mixing with  $\nu_\mu$ 's ( $\bar{\nu}_\mu$ 's), we did not show  $P(\bar{\nu}_e \rightarrow \nu_\tau, \bar{\nu}_\tau)$  and  $P(\nu_\mu \rightarrow \nu_\tau, \bar{\nu}_\tau)$ , which are almost the same as that for  $\nu_\mu, \bar{\nu}_\mu$ . We can see three clear conversions, one RSF and two MSWs. The RSF-H conversion occurs at  $r \sim 0.007R_\odot$  between  $\bar{\nu}_e$  and  $\nu_\tau$ . (The apparent  $\bar{\nu}_e \leftrightarrow \nu_\mu$  conversion occurs, since  $\nu_\mu$ 's are maximally mixing with  $\nu_\tau$ 's.) After that, neutrinos propagate in matter inducing the ordinary MSW effects, which are studied in detail by earlier authors [16, 17] (MSW-H at  $\sim 0.05R_\odot$ , MSW-L at  $\sim (0.2 - 0.5)R_\odot$ ). The strange behavior of  $P(\nu_\mu \rightarrow \bar{\nu}_e)$  at  $r \sim 0.04R_\odot$  is considered due to the nonadiabatic RSF-L conversion, while the probability is not changed as a whole.

Figure 6 is the same one as Fig. 5, but it is for  $\sin^2 2\theta_{13} = 10^{-6}$  instead of 0.04. In this case, we do not see the MSW-H conversion, since it is nonadiabatic.

We show in Fig. 7, the dependence of the conversion probability  $P(\nu_\mu \rightarrow \bar{\nu}_e)$  on the energy and the magnetic field strength at the iron core, assuming  $\sin^2 2\theta_{13} = 0.04$ . From Fig. 7 (a), we see that the resonance point goes to outer region and the conversion becomes more and more nonadiabatic, as the neutrino energy becomes larger. In the same manner, Fig. 7 (b) indicates that the conversion becomes more adiabatic for larger magnetic field strength. These behaviors can be understood qualitatively using Fig. 2 and Eq. (7).

At the end of this subsection, we compare the calculated conversion probabilities with ones which are evaluated with time-dependent density profile. Figure 8 shows  $P(\bar{\nu}_e \rightarrow \bar{\nu}_e)$  and  $P(\bar{\nu}_e \rightarrow \nu_{\mu,\tau})$  as a function of neutrino energy. Since how the shock propagation changes the structure of magnetic field at resonance points is not known well, we assume the same static dipole profile as for magnetic field, and the figure is for  $B_0 = 10^{10}$  G. As discussed in

Section III D, this assumption is considered to be a good one for  $\lesssim 0.5$  seconds after bounce, however, probably incorrect for  $> 0.5$  seconds. Anyway, from the figure, we can confirm that the probabilities are in good agreement between the model 0.5 sec and the static progenitor model.

### B. Energy spectrum at the SuperKamiokande detector

SK is a water Čerenkov detector with 32,000 tons of pure water based at Kamioka in Japan. The relevant interactions of neutrinos with water are as follows:

$$\bar{\nu}_e + p \rightarrow e^+ + n, \text{ (C.C.)} \quad (31)$$

$$\nu_e + e^- \rightarrow \nu_e + e^-, \text{ (C.C. and N.C.)} \quad (32)$$

$$\bar{\nu}_e + e^- \rightarrow \bar{\nu}_e + e^-, \text{ (C.C. and N.C.)} \quad (33)$$

$$\nu_x + e^- \rightarrow \nu_x + e^-, \text{ (N.C.)} \quad (34)$$

$$\nu_e + \text{O} \rightarrow e^- + \text{F}, \text{ (C.C.)} \quad (35)$$

$$\bar{\nu}_e + \text{O} \rightarrow e^+ + \text{N}, \text{ (C.C.)} \quad (36)$$

where C.C. and N.C. stand for charged- and neutral-current interactions, respectively.

SK is not in operation now because of the unfortunate accident, which occurred on 12th November 2001. However, it is expected to be repaired using remaining photomultiplier tubes (PMTs), and will restart the detection by the end of this year (2002) with lower performance. The effect of the accident on its performance is expected not to be serious for supernova neutrinos, because the fiducial volume will not change, and the threshold energy change (from 5 MeV to about 7-8 MeV) influences the event number very little. Although the energy resolution will become about  $\sqrt{2}$  times worse, it does not matter for our consideration. In the calculations, we used the energy threshold and the energy resolution after the accident.

For the reaction cross sections, we refer to Ref. [1]. The  $\bar{\nu}_e p$  is the largest reaction and the energy of recoil positrons is related to that of injected neutrinos by simple formula  $E_e = E_{\bar{\nu}_e} - (M_n - M_p) = E_{\bar{\nu}_e} - 1.29 \text{ MeV}$ , where  $M_n$ ,  $M_p$  are neutron and proton mass, respectively. The energy spectrum of electrons (positrons), therefore, reflects that of  $\bar{\nu}_e$ , which is easily estimated in some simple cases using e.g., Eqs. (24), (26), (28), and (30).

Figure 9 shows the energy spectra of electrons (positrons) for first 0.5 seconds evaluated with  $\sin^2 2\theta_{13} = 0.04$  and several values of  $B_0$ , which are calculated with conversion probabilities, original neutrino spectra, reaction cross sections, and detector performance. When we increase the value of  $B_0$ , the energy spectrum shifts to higher energy region and the shift saturates at  $B_0 \sim 10^{10}$  G. This is because at  $B_0 \gtrsim 10^9$  G the RSF-H conversion starts to become adiabatic and it achieves completely adiabatic transition at  $B_0 \sim 10^{10}$  G. For  $\sin^2 2\theta_{13} = 10^{-6}$ , we obtained almost the same figure as Fig. 9, and we do not show it here.

### C. Energy spectrum at the Sudbury Neutrino Observatory

SNO is a Čerenkov detector filled with 1,000 tons of heavy water. The interactions of neutrinos with heavy water are

$$\nu_e + d \rightarrow e^- + p + p, \text{ (C.C.)} \quad (37)$$

$$\bar{\nu}_e + d \rightarrow e^+ + n + n, \text{ (C.C.)} \quad (38)$$

$$\nu_x + d \rightarrow \nu_x + p + n, \text{ (N.C.)} \quad (39)$$

and reactions represented by Eqs. (32) to (36). Furthermore, the produced neutrons are detected through the interaction with surrounding nuclei as

$$n + d \rightarrow {}^3\text{H} + \gamma_{6.3}, \text{ (efficiency: 24\%)} \quad (40)$$

$$n + {}^{35}\text{Cl} \rightarrow {}^{36}\text{Cl} + \gamma_{8.6}, \text{ (efficiency: 83\%)} \quad (41)$$

where  $\gamma_{6.3}$  and  $\gamma_{8.6}$  represent the  $\gamma$ -rays whose energies are 6.3 MeV and 8.6 MeV, respectively, and NaCl is added to efficiently capture neutrons. Owing to these neutron capture reactions, the neutrino detection through the neutral-current reaction Eq. (39) is possible. Furthermore from the charged-current reaction of  $\bar{\nu}_e$ 's (Eq. (38)), we receive more than two signals, i.e., one from the preceding recoil positron, and the others from the delayed  $\gamma$ -rays by neutron captures. Thus, using this criterion, we can discern the  $\bar{\nu}_e d$  events from the other detection channels.

For the cross sections of reactions with deuterons, we referred to Ref. [47]. Figure 10 shows the energy spectra for first 0.5 seconds evaluated with  $\sin^2 2\theta_{13} = 0.04$  and several values of  $B_0$ <sup>3</sup>. The upper panel (a) shows the total energy spectra and the lower panel

---

<sup>3</sup> Since the neutral-current reaction Eq. (39) does not contribute to energy spectrum, we neglect it from

(b) the spectra of (total- $\bar{\nu}_e d$ ) events which can be obtained using the delayed coincidence signals, where the line types are the same as those used in Fig. 9. As  $B_0$  increases, the energy spectrum of the total events becomes harder, while that of the (total- $\bar{\nu}_e d$ ) events softer. These properties can be explained as follows. Since almost all the events come from  $\nu_e d$  and  $\bar{\nu}_e d$  reactions, the (total- $\bar{\nu}_e d$ ) events are roughly coincide with  $\nu_e d$  events. Thus, from the qualitative discussion given in Section IV, we can obtain the properties in Fig. 10 (b) (see Eqs. (23) and (27)). Since the energy spectrum due to  $\bar{\nu}_e d$  becomes harder for larger  $B_0$  (see Eqs. (24) and (28)), the total spectrum also becomes harder but with the suppressed degree of the shift, because that of the  $\nu_e d$  events relaxes.

Figure 11 is the same one as Fig. 10, but for the different value of  $\theta_{13}$  ( $\sin^2 2\theta_{13} = 10^{-6}$ ). For larger  $B_0$ , the spectrum of the total events becomes harder, while that of (total- $\bar{\nu}_e d$ ) events changes little (see Eqs. (25), (26), (29), and (30)).

## VI. DISCUSSION

In this study, we used the original neutrino spectrum calculated by Lawrence Livermore group [42]. Unfortunately, their study as well as the other published full numerical supernova collapse simulations have not yet included the nucleon bremsstrahlung process or nucleon recoils, even though it is no longer controversial that these effects are important. Recent studies (e.g. [48]) including all these processes have shown that average  $\nu_x$  energy exceeds the average  $\bar{\nu}_e$  energy by only a small amount, 10% being a typical number. If this is the case, the spectral deformation, particularly at SK detector, will be little and it is difficult to obtain some information on the flavor conversion mechanism in supernova. However, it is premature to conclude that their results are correct, since it is based on the neutrino transport study on the background of an assumed neutron star atmosphere, and this approach lacks hydrodynamical self-consistency. Further it is also because the mean energies and their ratios change significantly between the supernova bounce, accretion phase, and the later neutron star cooling phase.

Thus, at present, even if the Galactic supernova neutrino burst were detected by SK and SNO, it would be very difficult to obtain useful information on whether the RSF effect actu-

---

here on.



ally occurs in supernova and to obtain implication for neutrino magnetic moment, owing to large uncertainties concerning original neutrino spectrum. In the future, however, it might be plausible that these uncertainties will be removed by development of numerical simulations, and the signal of supernova neutrino burst would provide valuable implications for the flavor conversion mechanisms. In discussions from here, we present the method to probe conversion mechanisms from the detected neutrino signals, *assuming* that the uncertainties concerning the supernova models are considerably reduced by the future development of numerical approaches.

### A. Implication for neutrino magnetic moment

As we have shown in Section V, the deformation of spectral shape occurs when  $B_0 \gtrsim 10^9$  G. Therefore the ratio of high energy events to low energy ones is a good measure to investigate the magnetic field strength in supernova or neutrino magnetic moment. We adopted as that two quantities below:

$$R_{\text{SK}} = \frac{\text{Number of events for } E_e > 25 \text{ MeV}}{\text{Number of events for } E_e < 20 \text{ MeV}}, \quad (42)$$

$$R_{\text{SNO}} = \frac{\text{Number of events for } E_e > 25 \text{ MeV}}{\text{Number of events for } E_e < 15 \text{ MeV}}. \quad (43)$$

Figure 12 shows  $R_{\text{SK}}$  as a function of  $B_0 \sin \Theta$  for  $\sin^2 2\theta_{13} = 0.04$ , where error bars include only statistical errors. (Here, we re-introduce the angular factor  $\sin \Theta$  since we also discuss the dependence on magnetic field orientation below.) We obtained almost the same figure for  $\sin^2 2\theta_{13} = 10^{-6}$ . Therefore, SK data will provide statistically sufficient information on the magnetic field strength in the supernova and neutrino magnetic moment, and these consequences are independent of  $\theta_{13}$ . For example, the value of  $R_{\text{SK}}$  which is found to be larger than  $\sim 1$  indicates that the RSF conversion occurred in the supernova, and we can constrain the value of  $\mu_\nu B_0 \sin \Theta$  assuming the supernova and presupernova models.

The same figure for SNO is Fig. 13, where the upper panel (a) is for  $\sin^2 2\theta_{13} = 0.04$  and the lower panel (b) for  $\sin^2 2\theta_{13} = 10^{-6}$ . If we obtain  $R_{\text{SNO}}(\text{total})$  which is larger than  $R_{\text{SNO}}(\text{total} - \bar{\nu}_e \text{d})$ , it suggests that the supernova magnetic field is quite strong,  $B_0 \sin \Theta \gtrsim 5 \times 10^9 \text{G}$ , and neutrinos have non-zero magnetic moment. However, since the statistical errors of  $R_{\text{SNO}}$  are rather large because of smallness of data, we can use the SNO data to confirm the SK result.

In addition, if we know the value of the angular factor  $\sin \Theta$  from the optical observation such as the Hubble Space Telescope (HST), we can constrain the magnetic field strength  $B_0$  (not the combination  $B_0 \sin \Theta$ ) from the neutrino observation. Actually, in the case of SN1987A, which occurred in the Large Magellanic Cloud (LMC),  $\Theta$  is constrained with the procedure as follows. The HST images of SN1987A show a bright elliptical ring surrounding the optical remnant. This inner ring has been interpreted as a ring of high-density material in the equatorial plane of the progenitor, caused by the impact of the high velocity stellar wind of the blue supergiant progenitor with its earlier, slower red giant wind, and ionized by the UV flash from the supernova explosion [49]. The inner ring is known to be inclined to the line of sight by  $\sim 43^\circ$ . Thus, assuming that the magnetic dipole moment of the star orient to the rotation axis, we can constrain  $\sin \Theta$  to be  $\sim 1/\sqrt{2}$  from the HST observation. However, if the next supernova occurred in the Galactic center, it would be quite difficult to estimate  $\Theta$  since the Galactic center is optically thick from the Earth. On the other hand, if it occurred in the optically thin environment such as LMC, we would be able to constrain  $\Theta$  from optical observations and  $B_0$  from the neutrino signals. Although LMC is located at  $\sim 50$  kpc away from the Earth, SK data would permit statistically sufficient discussions on the supernova magnetic field. For example, in that case, the  $1\sigma$  statistical errors of  $R_{\text{SK}}$  are as large as  $5\sigma$  errors in the case of the Galactic supernova ( $D = 10$  kpc), which are also shown in Fig. 12, and it will be sufficient to distinguish whether  $B_0 \sin \Theta \gtrsim 5 \times 10^9$  G or  $B_0 \sin \Theta \lesssim 10^9$  G.

## B. Constraint from supernova relic neutrino observation

In addition to next Galactic supernova, the observation of supernova relic neutrino (SRN) background would be available to obtain information on flavor conversion mechanism in supernova. The flux of SRN is calculated by

$$\frac{dF_\nu}{dE_\nu} = c \int_0^{z_{\text{max}}} R_{\text{SN}}(z) \frac{dN_\nu(E'_\nu)}{dE'_\nu} (1+z) \frac{dt}{dz} dz, \quad (44)$$

where  $E'_\nu = (1+z)E_\nu$ ,  $R_{\text{SN}}(z)$  is supernova rate per comoving volume at redshift  $z$ ,  $dN_\nu/dE_\nu$  energy spectrum of emitted neutrinos, and  $z_{\text{max}}$  the redshift when the gravitational collapses began (see Ref. [50] for detailed discussion).

Most recently, SK collaboration set an upper bound of  $1.2 \bar{\nu}_e \text{ cm}^{-2} \text{ s}^{-1}$  for the SRN flux

in the energy region  $E_\nu > 19.3$  MeV [51]. That limit is the same order as some typical theoretical predictions such as Ref. [50]. For example, Ando et al. [50] predicted that the total SRN flux integrated over entire energy was  $11 \text{ cm}^{-2} \text{ s}^{-1}$ , while the corresponding SK limit calculated with the predicted spectral shape is  $31 \text{ cm}^{-2} \text{ s}^{-1}$ . Since the theoretical calculations contain many ambiguities such as the supernova rate in the universe and neutrino spectrum from each supernova, this severe observational SRN limit can provide a number of valuable information on the various fields of astrophysics and cosmology. Further, in the near future, it is expected that the upper limit will be much lower (about factor 3) when the current SK data of 1,496 days are reanalyzed using some technique to reduce background against detection [52]. In that case, the further severer constraint not only on the star formation history but also on the nature of neutrinos might be obtained.

Since the RSF mechanism further enhances the average energy of  $\bar{\nu}_e$  compared to the ordinary MSW effect, the current and the future expected upper limit on the SRN flux might provide very useful information on that mechanism. However, in order to give precise SRN prediction including the RSF mechanism, we must calculate conversion probability in supernova for full time-scale during the neutrino burst. Therefore, the prediction is difficult at present stage, and it is also one of our future works.

## VII. CONCLUSION

We investigated three-flavor neutrino oscillation with non-zero neutrino magnetic moment in supernova magnetic fields. We gave a new crossing diagram which includes not only ordinary MSW resonance but also magnetically-induced RSF effect. From the diagram, it was found that there occurred four resonances, two were induced by the RSF effect and two by the pure MSW. In addition, the qualitative behavior of neutrino conversions and expected neutrino spectrum at the detector were found to be well illustrated.

We also numerically calculated conversion probability in the supernova to obtain the expected energy spectrum at the detector. In that calculation, realistic neutrino mixing parameters inferred by recent neutrino oscillation experiments and realistic density and  $Y_e$  profiles of presupernova stars were adopted. As for magnetic field in the supernova, we assumed the dipole structure, and that the field strength was normalized at the surface of the iron core, which was inferred from the observations of white dwarfs. Although the

shock wave propagation changes density profile in the resonance region drastically and is also expected to change magnetic field profile at the same region, we showed that if we confine our discussion until 0.5 seconds after core bounce, using static progenitor model and static magnetic field structure is expected to be a good approximation.

As a result of numerical calculations, it was found that if the magnetic field at the surface of the iron core is sufficiently strong ( $B_0 \sim 10^{10}\text{G}$ , where we assumed  $\mu_\nu = 10^{-12} \mu_B$ ), the RSF-H conversion becomes adiabatic and complete  $\bar{\nu}_e \leftrightarrow \nu_\tau$  conversion occurs. Hence, non-zero neutrino magnetic moment with the strong magnetic field enhances the energies of  $\bar{\nu}_e$  and hardens the energy spectrum at SK and SNO. Thus, in the future, if the uncertainty concerning original neutrino spectrum is removed by development of numerical simulations for supernova explosions, we might be able to obtain information on neutrino magnetic moment as well as the magnetic field strength in supernova using the energy spectrum at detectors. In addition, it could be also plausible using the current and the future supernova relic neutrino observations.

### Acknowledgments

We would like to thank SuperKamiokande collaboration including Y. Suzuki, M. Nakahata, Y. Fukuda, and A. Suzuki for useful discussion on supernova relic neutrino background. This work was supported in part by grants-in-aid for scientific research provided by the Ministry of Education, Science and Culture of Japan through Research grant no. S14102004.

- 
- [1] Y. Totsuka, Rep. Prog. Phys. **55**, 377 (1992); K. Nakamura, T. Kajita, and A. Suzuki, in *Physics and Astrophysics of Neutrinos*, edited by M. Fukugita and A. Suzuki (Springer-Verlag, Tokyo, 1994), p. 249.
  - [2] J. Boger et al., Nucl. Inst. Meth. A **449**, 172 (2000).
  - [3] S. Fukuda et al., Phys. Rev. Lett. **86**, 5656 (2001).
  - [4] J. N. Bahcall, P. I. Krastev, A. Yu. Smirnov, Phys. Rev. D **58**, 096016 (1998).
  - [5] Q. R. Ahmad et al., Phys. Rev. Lett. **87**, 071301 (2001).
  - [6] Q. R. Ahmad et al., Phys. Rev. Lett. **89**, 011301 (2002); Phys. Rev. Lett. **89**, 011302 (2002).
  - [7] Y. Fukuda et al., Phys. Rev. Lett. **82**, 2644 (1999); K. Scholberg, hep-ex/9905016.

- [8] T. Kajita and Y. Totsuka, *Rev. Mod. Phys.* **73**, 85 (2001).
- [9] M. Apollonio et al., *Phys. Lett. B* **466**, 415, 1999.
- [10] K. Hirata et al., *Phys. Rev. Lett.* **58**, 1490 (1987).
- [11] R. M. Bionta et al., *Phys. Rev. Lett.* **58**, 1494 (1987).
- [12] K. Sato and H. Suzuki, *Phys. Rev. Lett.* **58**, 2722 (1987).
- [13] J. Arafune and M. Fukugita, *Phys. Rev. Lett.* **59**, 367 (1987).
- [14] I. Goldman et al., *Phys. Rev. Lett.* **60**, 1789 (1988).
- [15] G. G. Raffelt, *Nucl. Phys. B (Proc. Suppl.)* **110**, 254 (2002).
- [16] A. S. Dighe and A. Yu. Smirnov, *Phys. Rev. D* **62**, 033007 (2000).
- [17] K. Takahashi, M. Watanabe, K. Sato, and T. Totani, *Phys. Rev. D* **64**, 093004 (2001); K. Takahashi and K. Sato, hep-ph/0205070.
- [18] A. Ayala, J. C. D’Olivo, and M. Torres, *Phys. Rev. D* **59**, 111901 (1999).
- [19] A. I. Derbin et al., *JETP Lett.* **57**, 768 (1993) [*Pis'ma Zh. Eksp. Teor. Fiz.* **57**, 755 (1993)].
- [20] S. N. Gninenko, *Phys. Lett. B* **452**, 414 (1999); *Mod. Phys. Lett. A* **13**, 1791 (1998); *Phys. Lett. B* **427**, 206 (1998); S. N. Gninenko and N. V. Krasnikov, *Phys. Lett. B* **490**, 9 (2000).
- [21] J. F. Beacom and P. Vogel, *Phys. Rev. Lett.* **83**, 5222 (1999).
- [22] A. Joshipura and S. Mohanty, *Phys. Rev. D* **66**, 012003 (2002).
- [23] G. G. Raffelt, *Phys. Rev. Lett.* **64**, 2856 (1990); *Astrophys. J* **365**, 559 (1990); *Phys. Rept.* **320**, 319 (1999).
- [24] M. Fukugita and T. Yanagida, *Phys. Rev. Lett.* **58**, 1807 (1987); K. S. Babu and V. S. Mathur, *Phys. Lett. B* **196**, 218 (1987).
- [25] A. Cisneros, *Astrophys. Space Sci.* **10**, 87 (1970).
- [26] K. Fujikawa and R. E. Shrock, *Phys. Rev. Lett.* **45**, 963 (1980).
- [27] J. Schechter and J. W. F. Valle, *Phys. Rev. D* **24**, 1883 (1981); **25**, 283(E) (1982).
- [28] C. S. Lim and W. J. Marciano, *Phys. Rev. D* **37**, 1368 (1988).
- [29] L. Wolfenstein, *Phys. Rev. D* **17**, 2369 (1978); S. P. Mikheyev and A. Yu. Smirnov, *Yad. Fiz.* **42**, 1441 (1985) [*Sov. J. Nucl. Phys.* **42**, 913 (1985)]; *Nuovo Climento C* **9**, 17 (1986).
- [30] T. K. Kuo and J. Pantaleone, *Rev. Mod. Phys.* **61**, 937 (1989).
- [31] E. Kh. Akhmedov, *Yad. Fiz.* **48**, 599 (1988) [*Sov. J. Nucl. Phys.* **48**, 382 (1988)]; *Phys. Lett. B* **213**, 64 (1988).
- [32] M. B. Voloshin, *Phys. Lett. B* **209**, 360 (1988).

- [33] E. Kh. Akhmedov and Z. G. Berezhiani, Nucl. Phys. B **373**, 479 (1992); E. Kh. Akhmedov, S. T. Petcov, and A. Yu. Smirnov, Phys. Rev. D **48**, 2167 (1993).
- [34] J. T. Peltoniemi, Astron. Astrophys. **254**, 121 (1992).
- [35] H. Athar, J. T. Peltoniemi, and A. Yu. Smirnov, Phys. Rev. D **51**, 6647 (1995).
- [36] T. Totani and K. Sato, Phys. Rev. D **54**, 5975 (1996).
- [37] H. Nunokawa, Y. Z. Qian, and G. M. Fuller, Phys. Rev. D **55**, 3265 (1997); H. Nunokawa, R. Tomàs, and J. W. F. Valle, Astropart. Phys. **11**, 317 (1999).
- [38] S. Esposito, V. Fiorentino, G. Mangano, and G. Miele, Z. Phys. C **76**, 479 (1997).
- [39] J. M. Lattimer and J. Cooperstein, Phys. Rev. Lett. **61**, 23 (1988); R. Barbieri and R. N. Mohapatra, Phys. Rev. Lett. **61**, 27 (1988); D. Nötzold, Phys. Rev. D **38**, 1658 (1988).
- [40] J. Pulido and E. Kh. Akhmedov, Astropart. Phys. **13**, 227 (2000); J. Pulido, hep-ph/0106201.
- [41] J. R. Wilson, R. Mayle, S. Woosley, and T. Weaver, Ann. N. Y. Acad. Sci. **470**, 267 (1986).
- [42] T. Totani, K. Sato, H. E. Dalhed, and J. R. Wilson, Astrophys. J. **496**, 216 (1998).
- [43] S. E. Woosley and T. A. Weaver, Astrophys. J. Suppl. **101**, 181 (1995).
- [44] R.C. Schirato and G.M. Fuller, astro-ph/0205390.
- [45] K. Takahashi, K. Sato, H.E. Dalhed, J.R. Wilson, in preparation.
- [46] G. Chanmugam, Ann. Rev. Astron. Astrophys. **411**, 823 (1993).
- [47] S. Ying, W. C. Haxton, and E. M. Henley, Phys. Rev. D **40**, 3211 (1989).
- [48] M. Th. Keil, G. G. Raffelt, and H. T. Janka, astro-ph/0208035.
- [49] C. J. Burrows et al., Astrophys. J. **452**, 680 (1995).
- [50] S. Ando, K. Sato, and T. Totani, astro-ph/0202450, to appear in Astroparticle Physics; S. Ando and K. Sato, astro-ph/0210502.
- [51] M. Malek et al., SuperKamiokande collaboration, hep-ex/0209028.
- [52] Y. Suzuki, private communication.

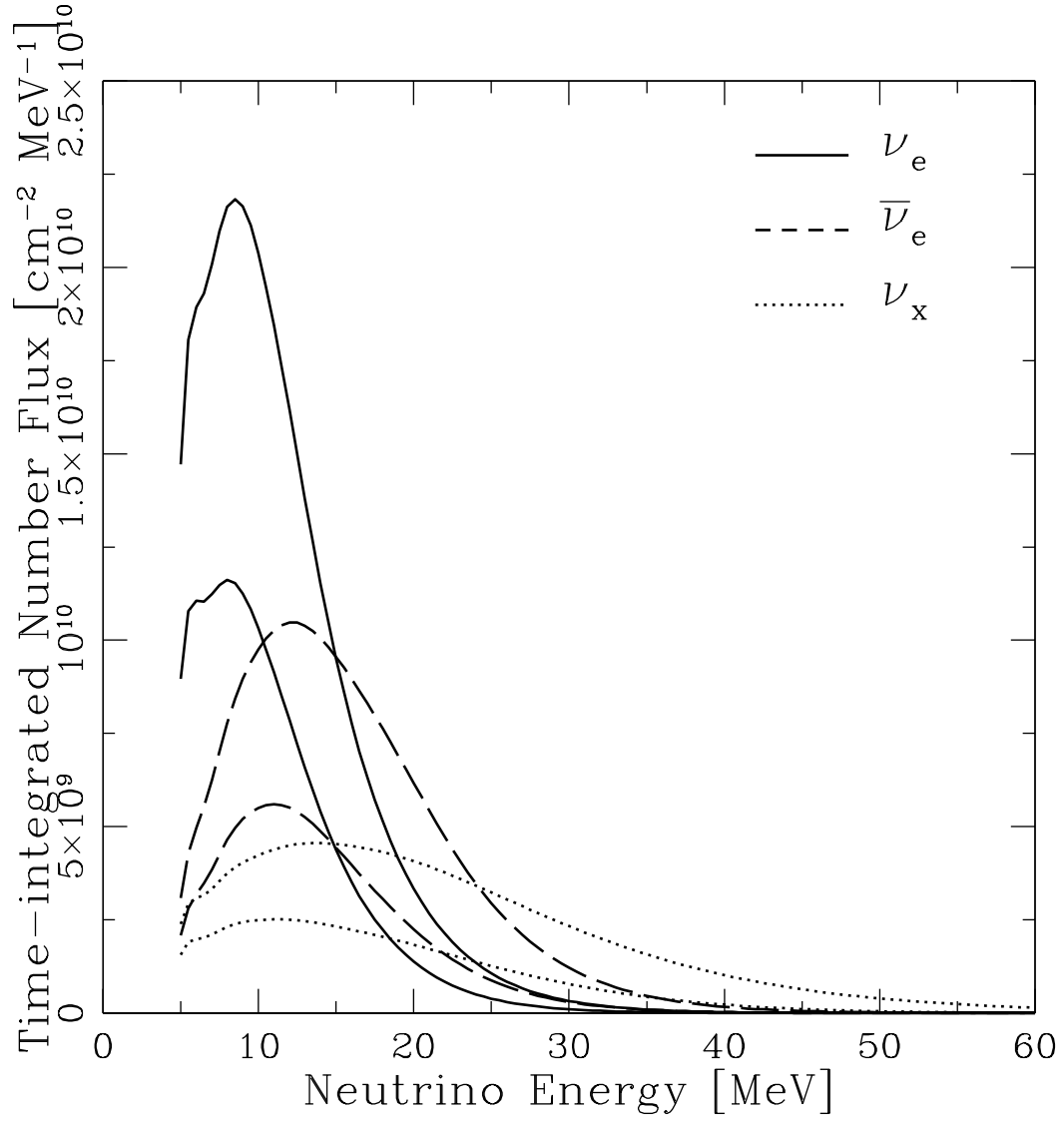


FIG. 1: Original time-integrated energy spectra of  $\nu_e$  (solid curve),  $\bar{\nu}_e$  (dashed curve), and  $\nu_x$  (dotted curve), where  $\nu_x$  represents  $\nu_{\mu,\tau}$  and  $\bar{\nu}_{\mu,\tau}$ . For each line type, the larger one represents fully time-integrated spectrum, while smaller one spectrum integrated until 0.5 seconds after core bounce.

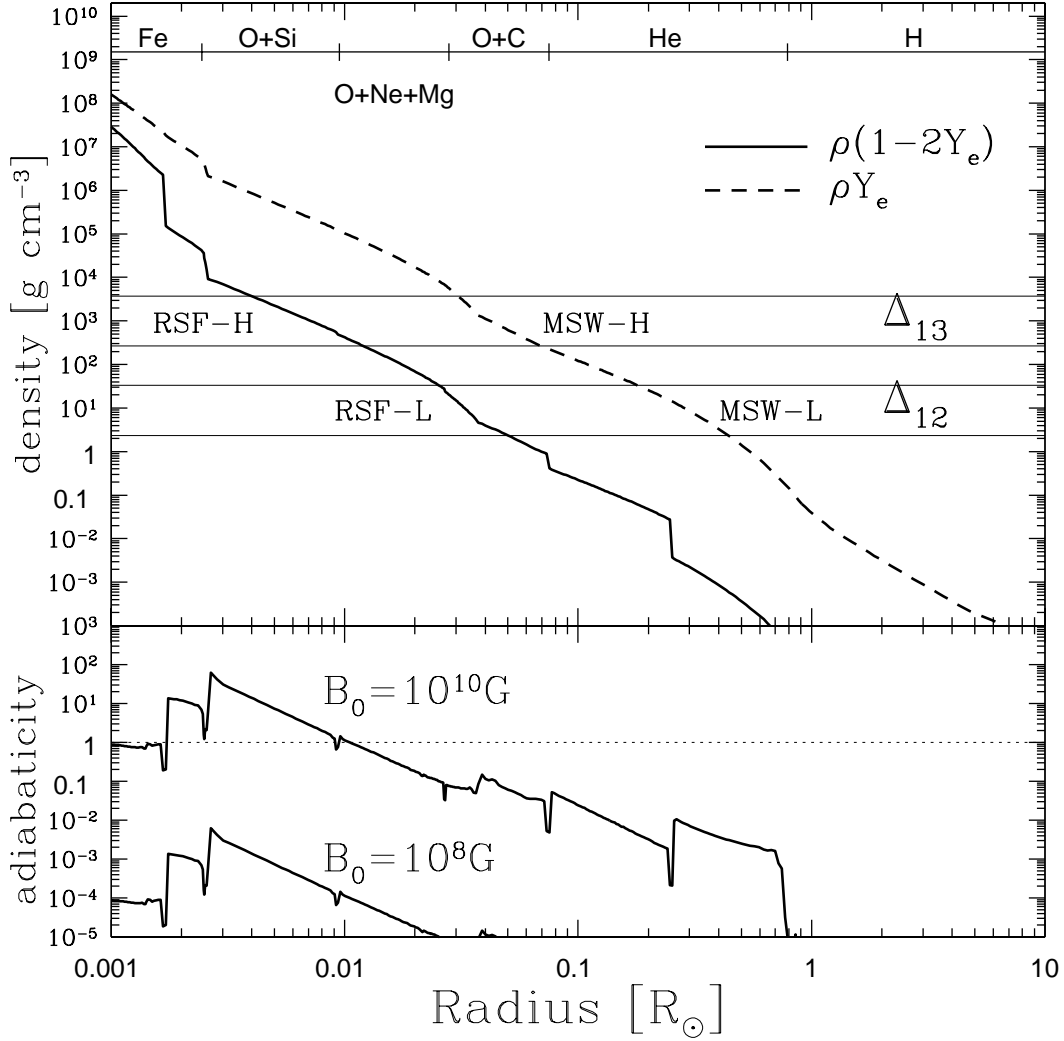


FIG. 2: Supernova profiles used in our calculations [43]. Upper panel: The solid curve represents the density and  $Y_e$  combination which is responsible for the RSF conversions ( $\rho(1 - 2Y_e)$ ), and the dashed curve for the MSW conversions ( $\rho Y_e$ ). Two horizontal bands are for  $\Delta_{12} = \Delta m_{12}^2 \cos 2\theta_{12}/2\sqrt{2}G_F E_\nu$  and  $\Delta_{13} = \Delta m_{13}^2 \cos 2\theta_{13}/2\sqrt{2}G_F E_\nu$ . (The band width comes from the energy range 5-70 MeV.) At intersections between the solid, dashed curves and the horizontal bands, the RSF and MSW conversions occur (see Eq. (6)). Lower panel: The adiabaticity parameter of RSF conversions (Eq. (7)) as a function of radius, where the indicated values are magnetic field strength at the iron core ( $B_0$ ) when  $\mu_\nu = 10^{-12} \mu_B$  is assumed.



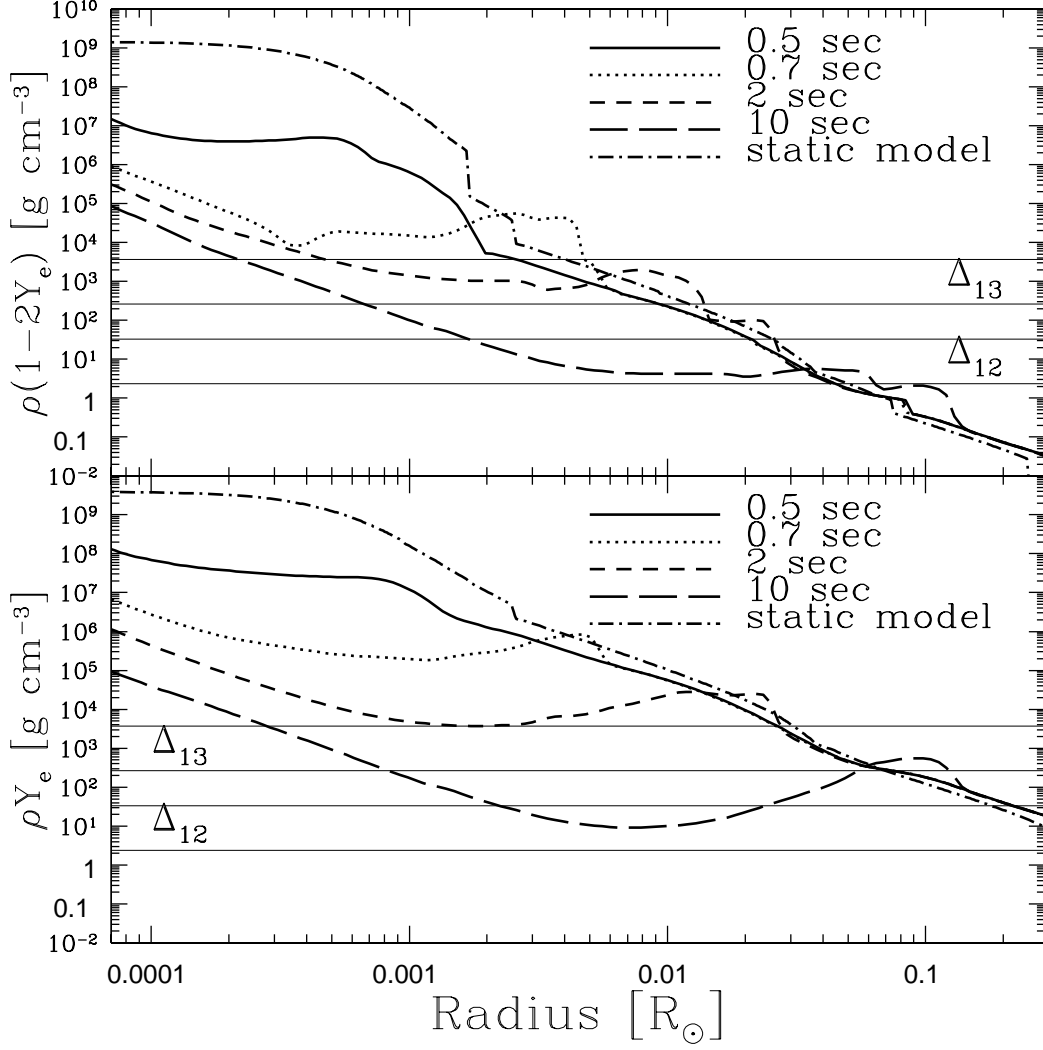


FIG. 3: Time-dependent density and  $Y_e$  profiles of supernova calculated by Lawrence Livermore group [45]. Upper panel: The  $\rho(1 - 2Y_e)$  profile of supernova, which is responsible for RSF conversions. The profile at 0.5, 0.7, 2, and 10 seconds after bounce, are shown. The profile calculated with static progenitor model [43] is also shown, for comparison. The resonance points, which are represented by the intersections between the  $\rho(1 - 2Y_e)$  curves and horizontal bands ( $\Delta_{13}, \Delta_{12}$ ), are affected by the shock propagation at  $> 0.5$  seconds. Lower panel: The same figure, but for  $\rho Y_e$  profile, which is responsible for MSW conversions.

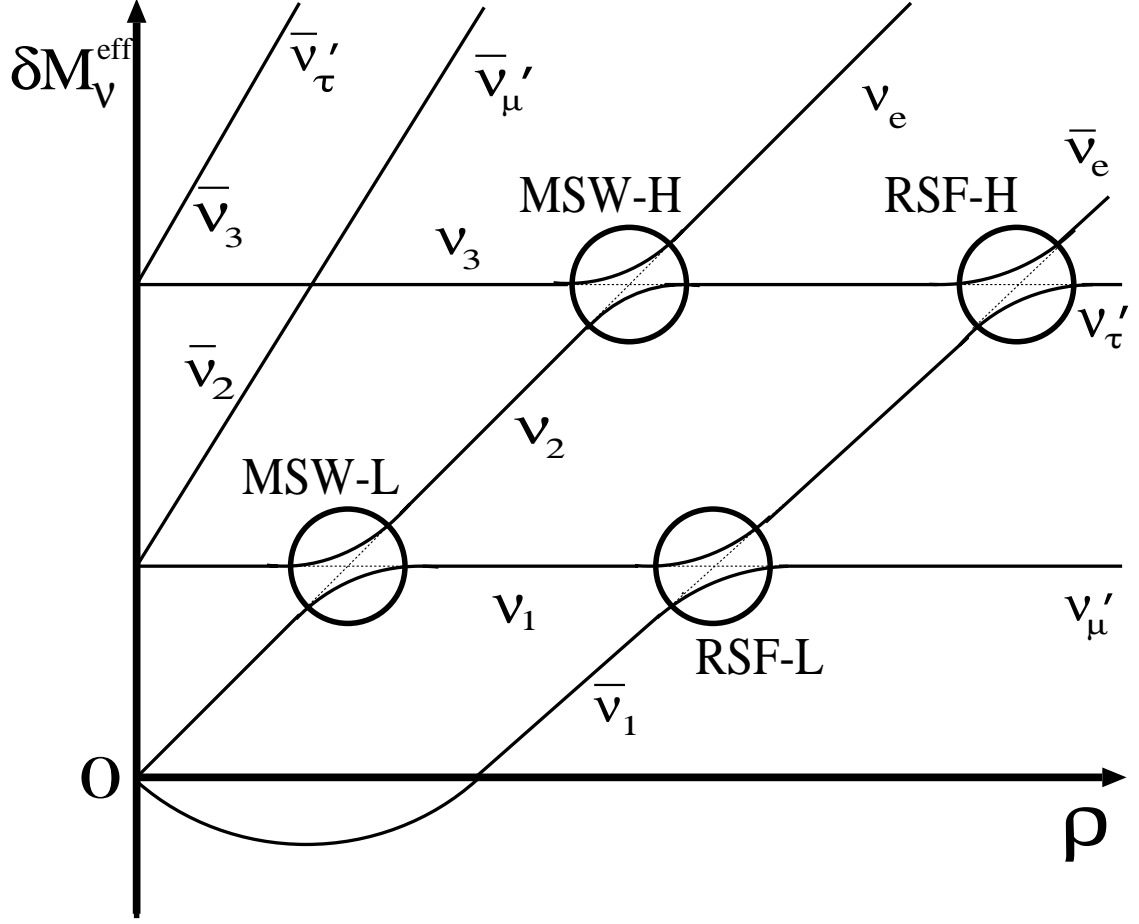


FIG. 4: The schematic illustration of level crossings, where  $\nu_{1,2,3}$  and  $\bar{\nu}_{1,2,3}$  represent the mass eigenstates of neutrinos and anti-neutrinos in matter, respectively, and  $\nu'_{\mu,\tau}$  and  $\bar{\nu}'_{\mu,\tau}$  the mass eigenstates at production, which are superpositions of  $\nu_\mu$  and  $\nu_\tau$  or  $\bar{\nu}_\mu$  and  $\bar{\nu}_\tau$ . There are four resonance points, MSW-L, MSW-H, RSF-L, and RSF-H. The adiabatic conversion means that the neutrinos trace the solid curve at each resonance point (i.e., the mass eigenstate does not flip), while the nonadiabatic conversion the dotted line.

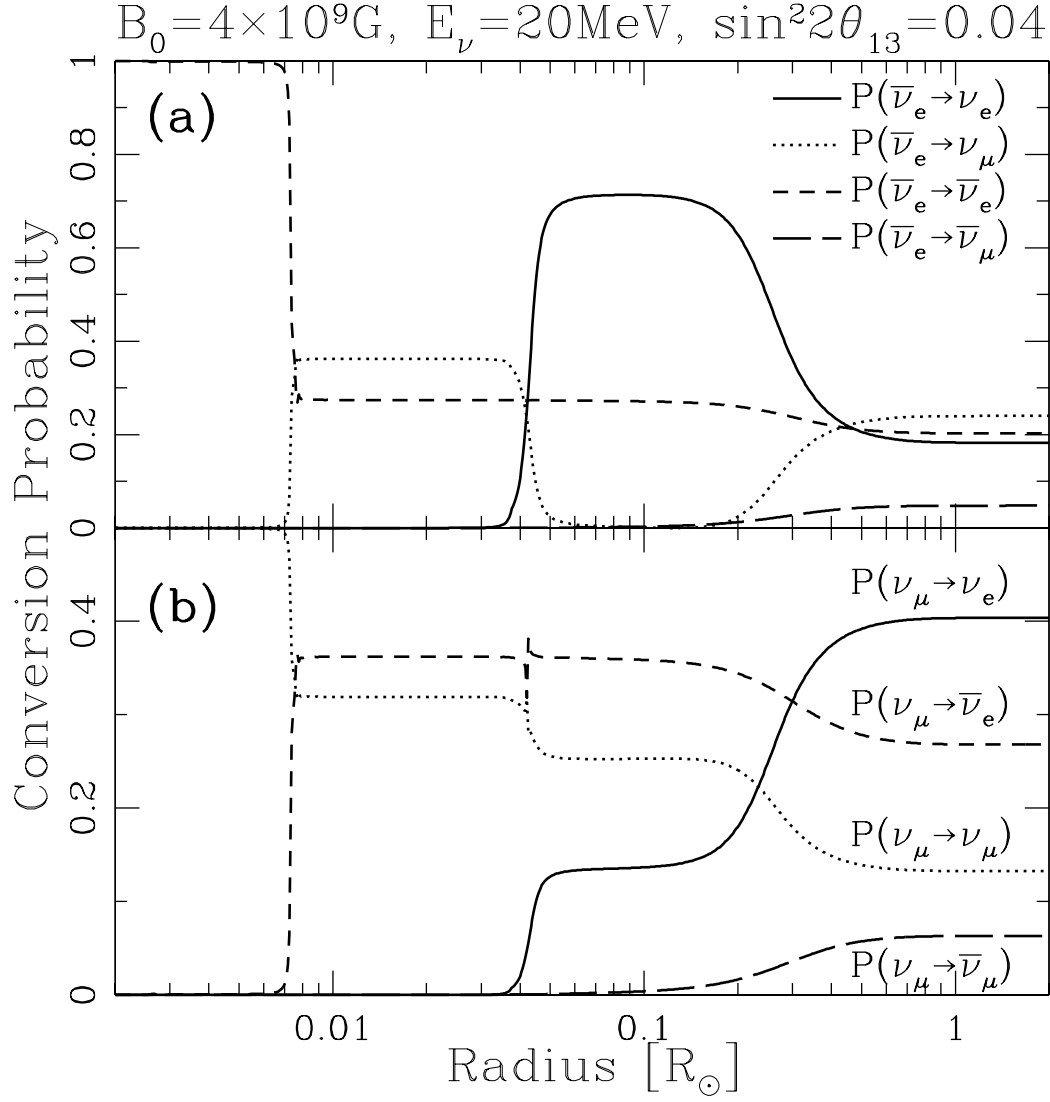


FIG. 5: (a) Conversion probabilities of  $\bar{\nu}_e$  under the condition that  $B_0 = 4 \times 10^9 \text{G}$ ,  $E_\nu = 20 \text{MeV}$ , and  $\sin^2 2\theta_{13} = 0.04$ . The solid curve represents  $P(\bar{\nu}_e \rightarrow \nu_e)$ , the dotted curve  $P(\bar{\nu}_e \rightarrow \nu_\mu)$ , the short-dashed curve  $P(\bar{\nu}_e \rightarrow \bar{\nu}_e)$ , and the long-dashed curve  $P(\bar{\nu}_e \rightarrow \bar{\nu}_\mu)$ . (b) The same figure as (a), but for those of  $\nu_\mu$ . The solid curve represents  $P(\nu_\mu \rightarrow \nu_e)$ , the dotted curve  $P(\nu_\mu \rightarrow \nu_\mu)$ , the short-dashed curve  $P(\nu_\mu \rightarrow \bar{\nu}_e)$ , and the long-dashed curve  $P(\nu_\mu \rightarrow \bar{\nu}_\mu)$ .

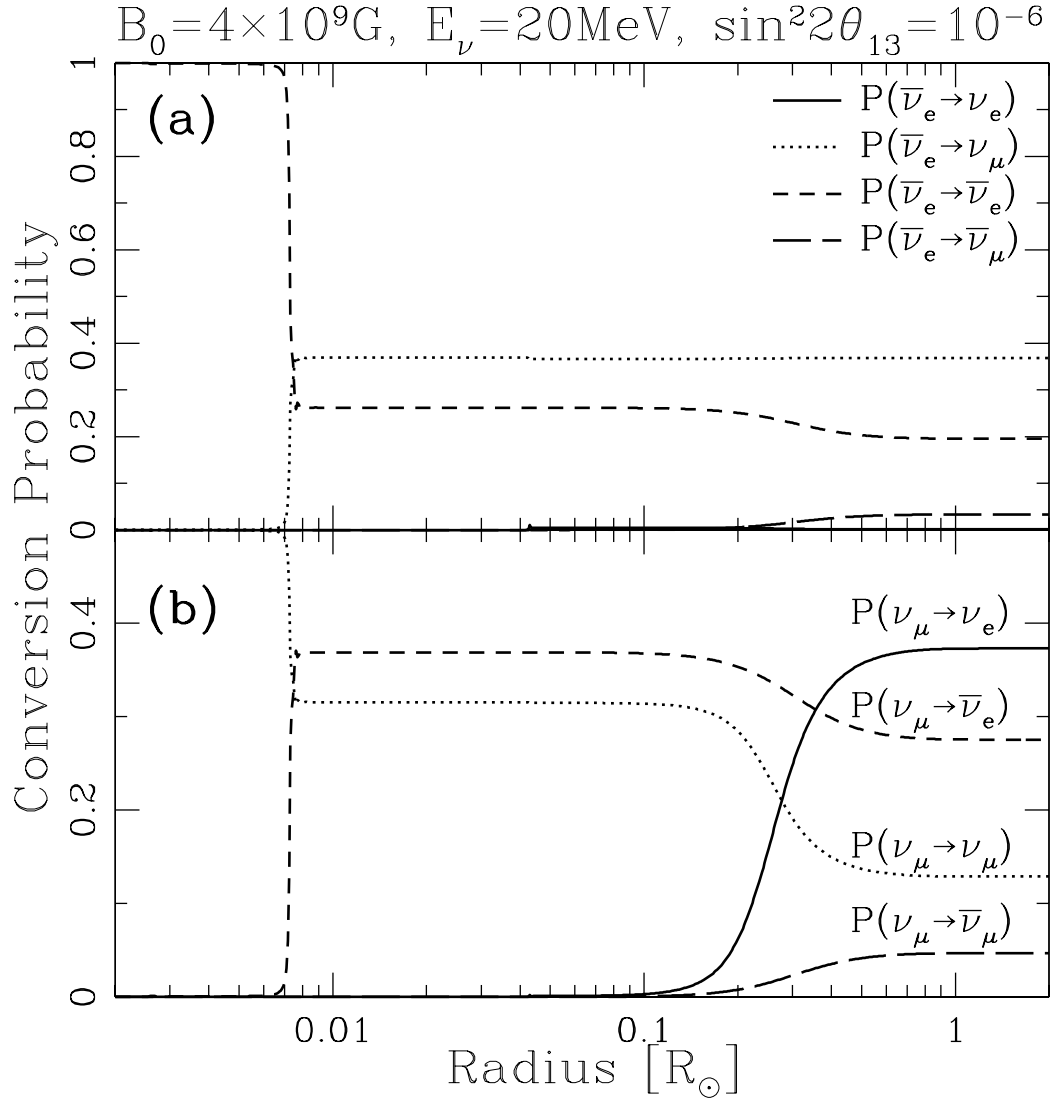


FIG. 6: The same figure as Fig. 5, but for  $\sin^2 2\theta_{13} = 10^{-6}$ .

$\sin^2 2\theta_{13} = 0.04$ ; (a)  $B_0 = 2 \times 10^9 \text{ G}$ , (b)  $E_\nu = 25 \text{ MeV}$

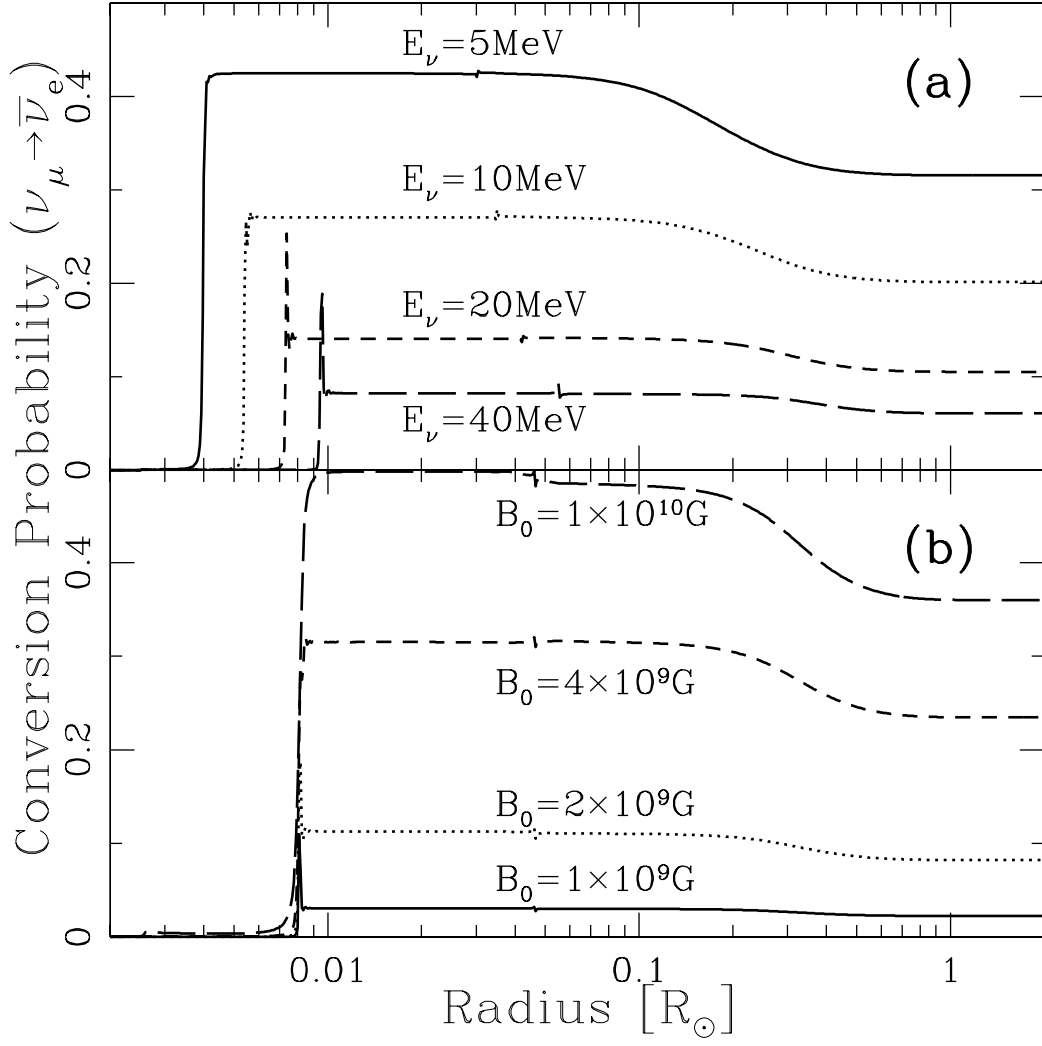


FIG. 7: Conversion probability  $P(\nu_\mu \rightarrow \bar{\nu}_e)$  for  $\sin^2 2\theta_{13} = 0.04$ . (a) The energy dependence for  $B_0 = 2 \times 10^9 \text{ G}$ . (b) The dependence on the magnetic field strength at the iron core, for  $E_\nu = 25 \text{ MeV}$ .

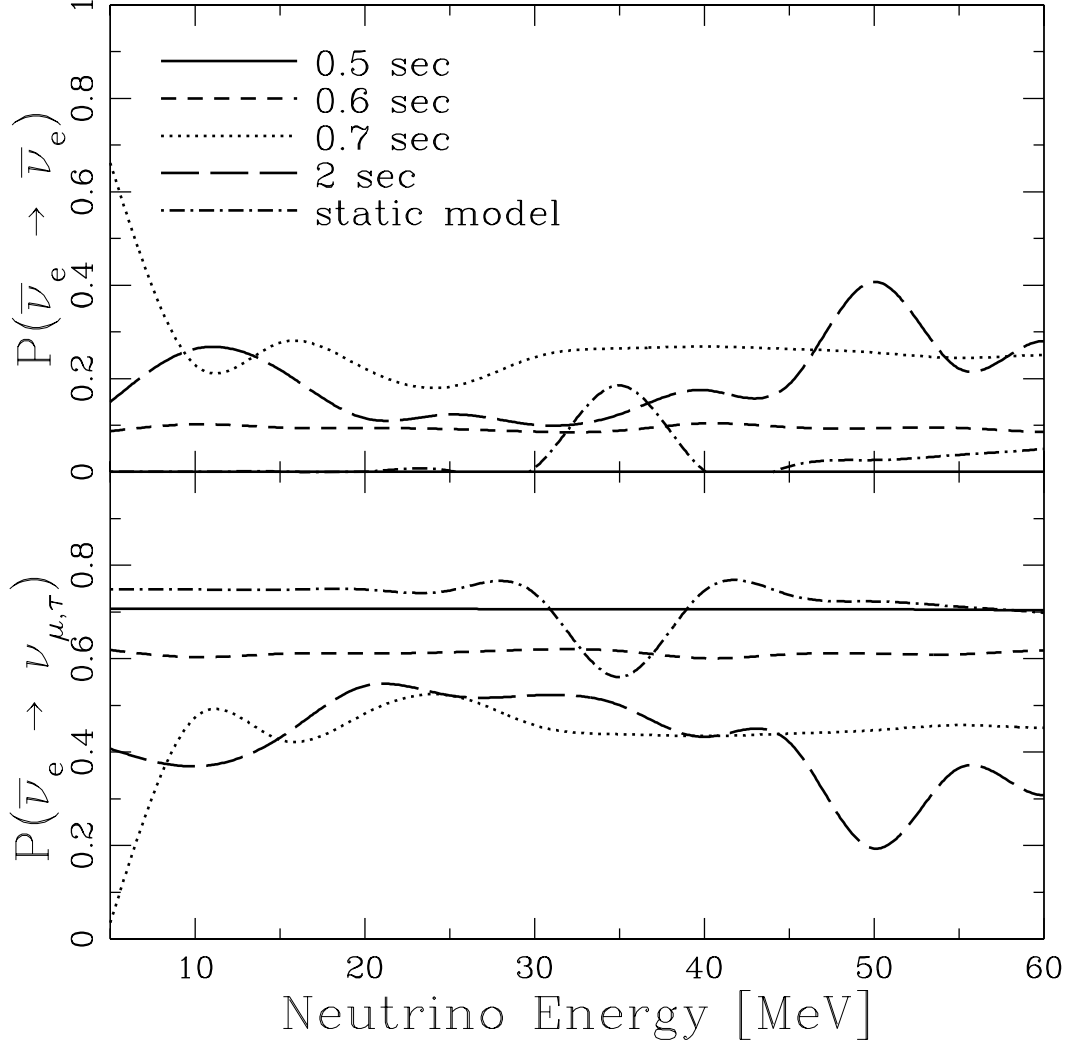


FIG. 8: The conversion probability  $P(\bar{\nu}_e \rightarrow \bar{\nu}_e)$  and  $P(\bar{\nu}_e \rightarrow \nu_{\mu,\tau})$  as a function of neutrino energy, which are evaluated with time-dependent density and  $Y_e$  profiles at 0.5 (solid line), 0.6 (short-dashed line), 0.7 (dotted line), and 2 (long-dashed line) seconds after bounce. Those obtained with static progenitor model is also shown as dot-dashed line. The magnetic field profile is assumed to be the same one as the static dipole model ( $B_0 = 10^{10}$  G).

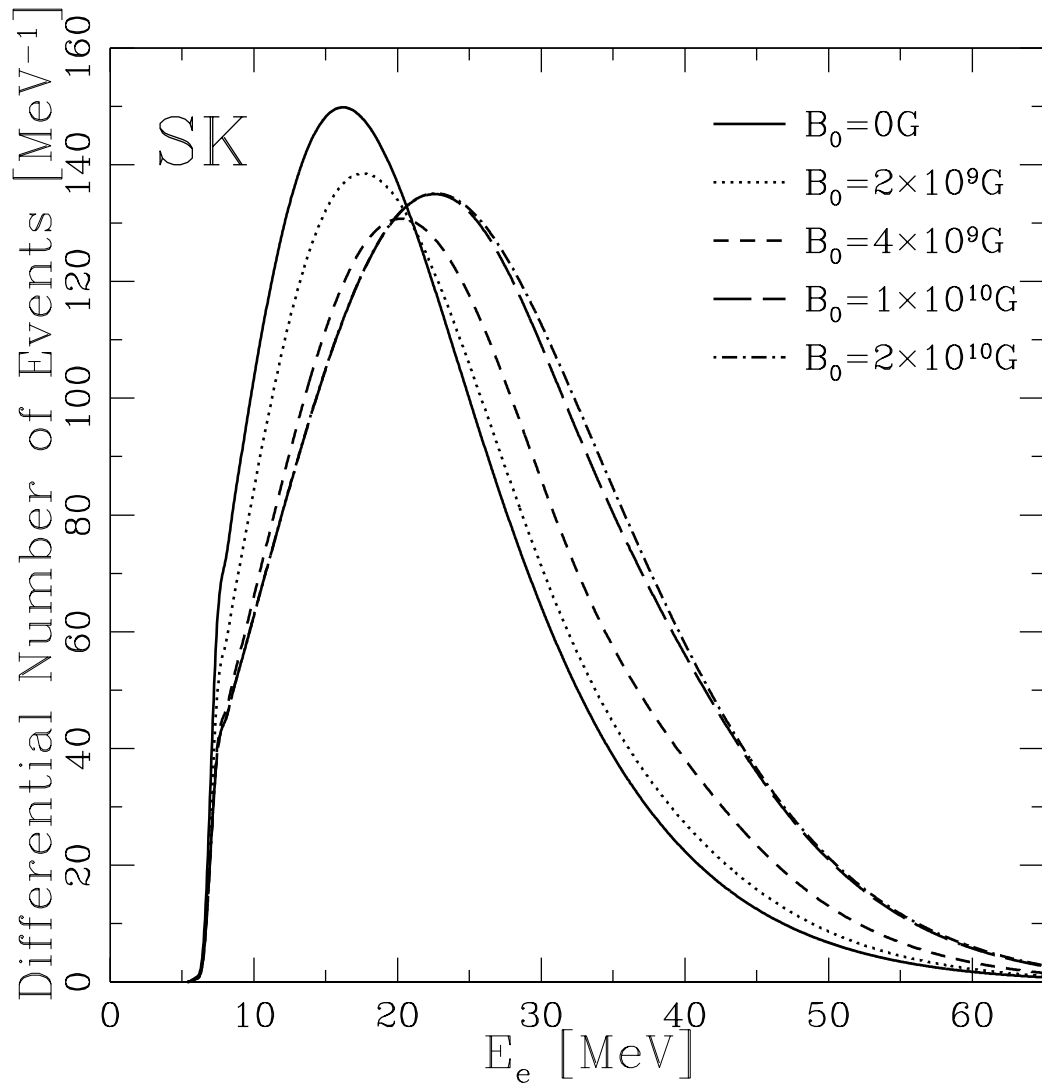


FIG. 9: Energy spectra of electrons (positrons) at SK for first 0.5 seconds, evaluated with  $\sin^2 2\theta_{13} = 0.04$  and several values of  $B_0$ . The energy spectra for  $\sin^2 2\theta_{13} = 10^{-6}$  are almost the same. The mean energy increases as  $B_0$  becomes larger, and saturates around  $B_0 = 10^{10}$  G (completely adiabatic RSF-H conversion).

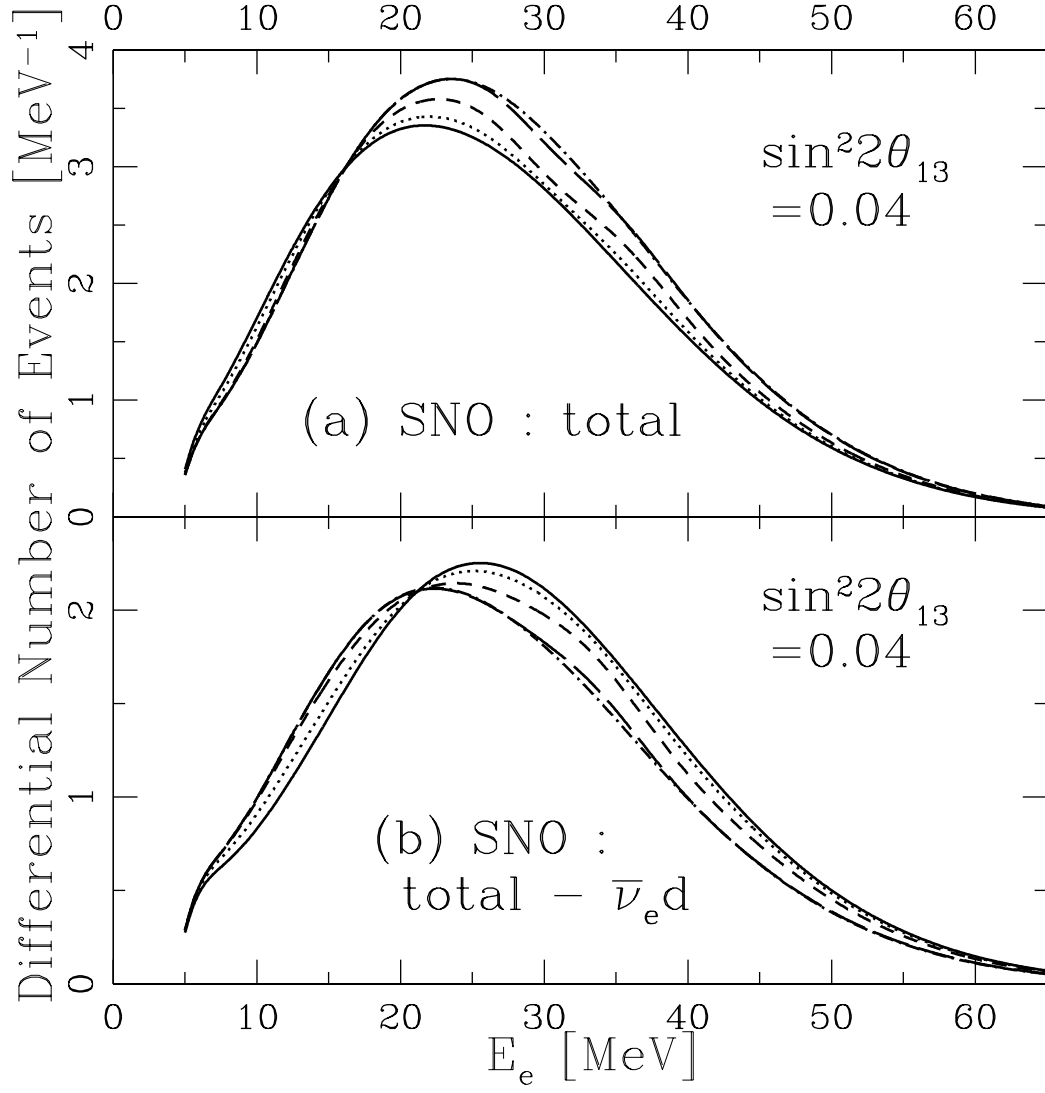


FIG. 10: Energy spectra at SNO for first 0.5 seconds evaluated with  $\sin^2 2\theta_{13} = 0.04$  and several values of  $B_0$ . The line types are the same as those used in Fig. 9. (a) Total numbers of events at SNO. As  $B_0$  increases, the spectrum becomes harder. (b) Numbers of events at SNO, where the  $\bar{\nu}_e d$  events (Eq. (38)) are subtracted from the total events. The spectrum moves conversely compared to the total events (a), as the values of  $B_0$ .



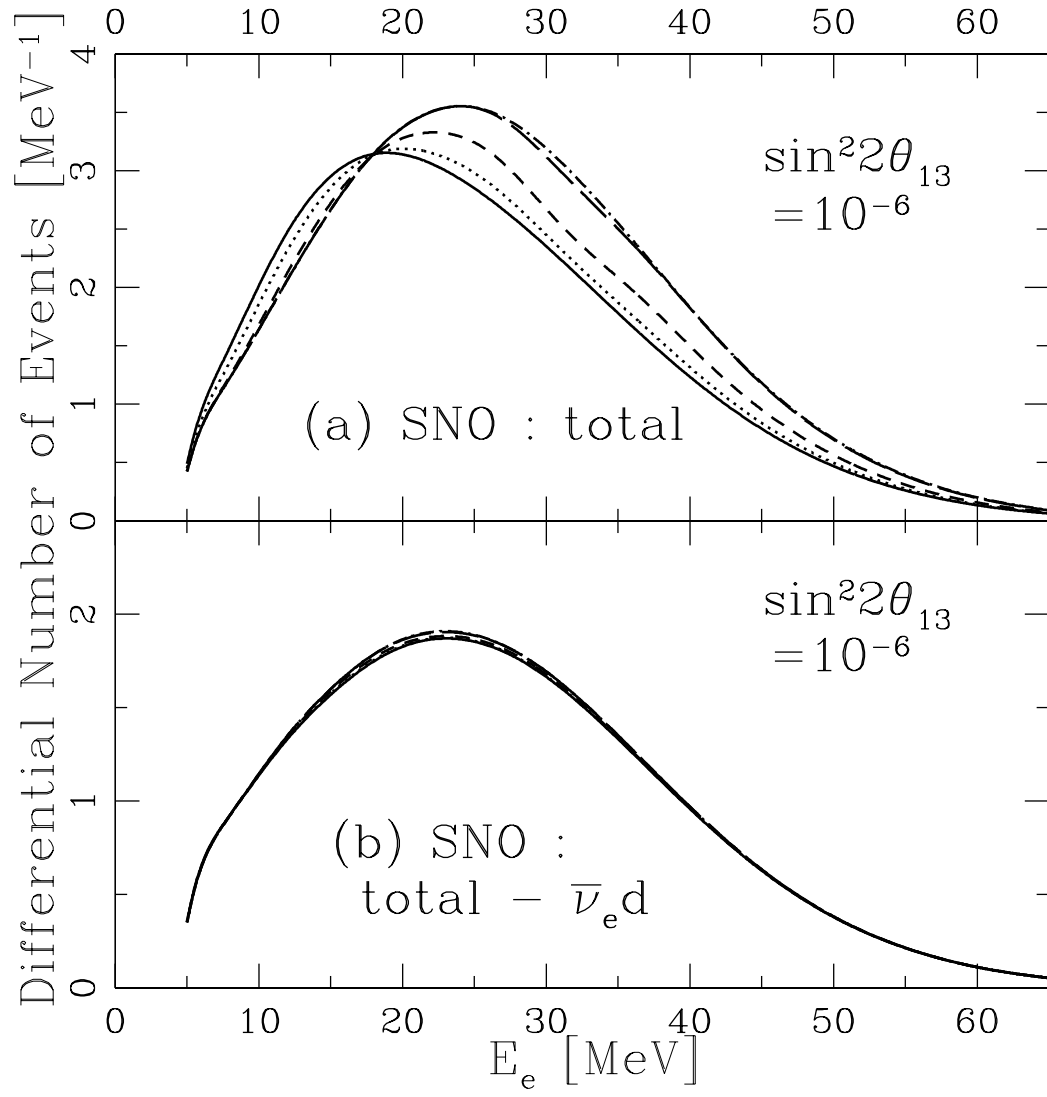


FIG. 11: The same figure as Fig. 10, but for  $\sin^2 2\theta_{13} = 10^{-6}$ . For larger  $B_0$ , the spectrum of the total events (a) becomes harder, while that of (total- $\bar{\nu}_e d$ ) events (b) changes little.

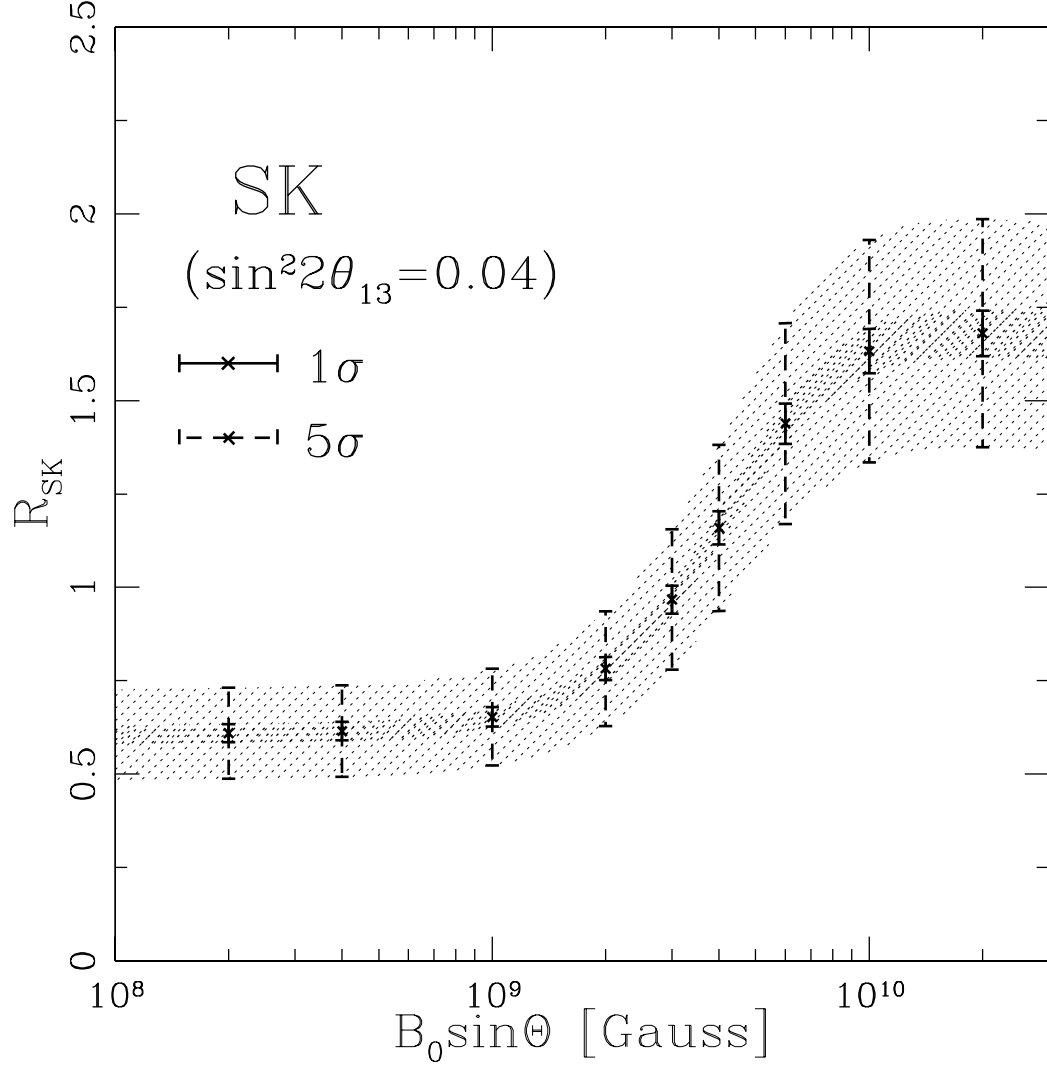


FIG. 12: Ratio of high energy events to low energy events at SK,  $R_{\text{SK}}$ , as a function of  $B_0 \sin \Theta$  for  $\sin^2 2\theta_{13} = 0.04$ , where error bars include only statistical errors. The solid error bars are at  $1\sigma$  level and the dashed ones at  $5\sigma$  level. The thick and thin bands are the cubic spline interpolations of  $1\sigma$  and  $5\sigma$  error bars, respectively.

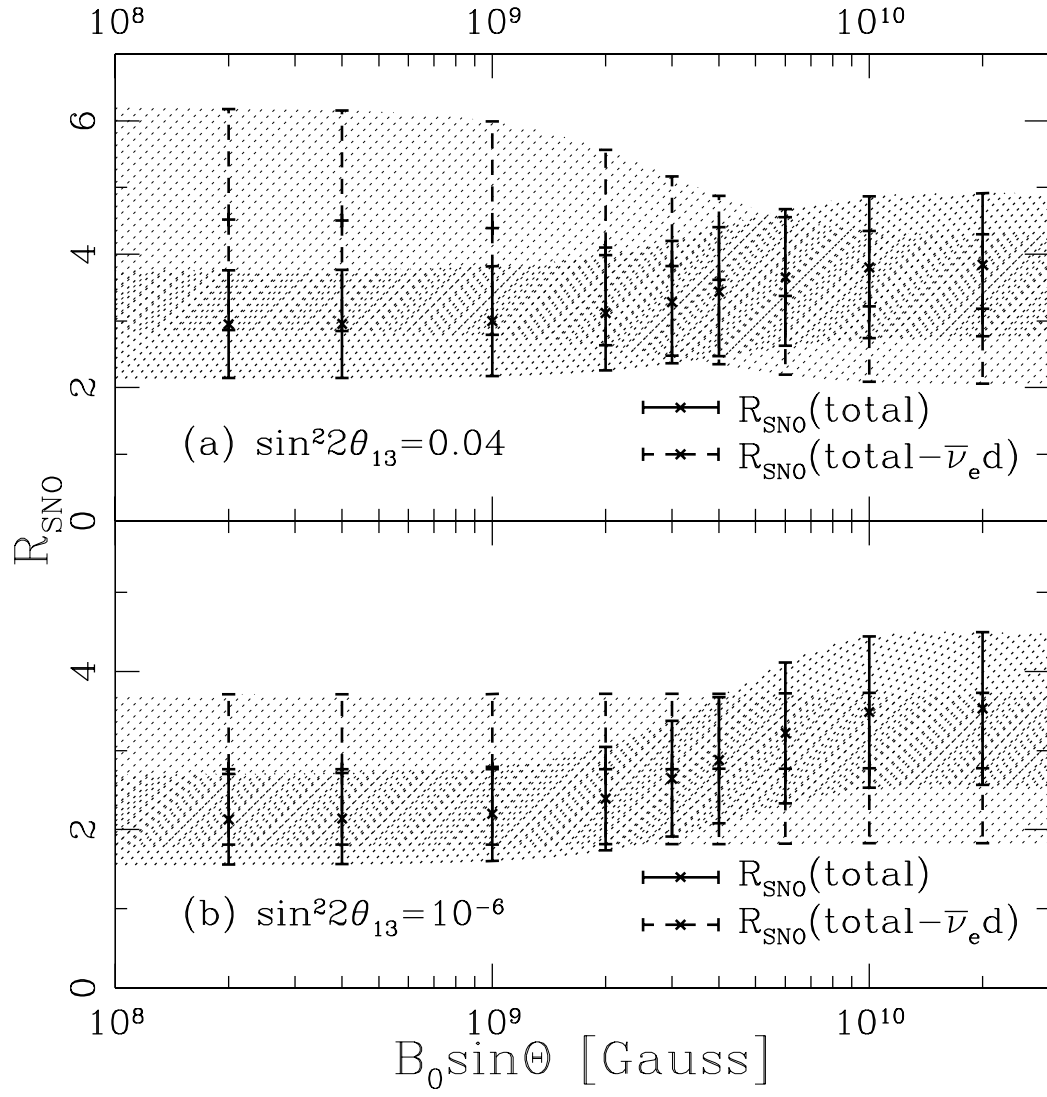


FIG. 13: Ratio of high energy events to low energy events at SNO,  $R_{\text{SNO}}$ , where the upper panel (a) is for  $\sin^2 2\theta_{13} = 0.04$  and the lower panel (b) for  $\sin^2 2\theta_{13} = 10^{-6}$ . The error bars include only statistical errors, and are at  $1\sigma$  level. The thick and thin bands are the cubic spline interpolations of these error bars.